

**Practical and improved density functionals for computational catalysis  
on metal surfaces**

Benjamin X. Shi<sup>1,\*</sup> and Timothy C. Berkelbach<sup>1,2,\*</sup>

<sup>1</sup>*Initiative for Computational Catalysis,*

*Flatiron Institute, New York, NY 10010, USA*

<sup>2</sup>*Department of Chemistry, Columbia University, New York, NY 10027, USA*

(Dated: February 17, 2026)

## Abstract

Density functional theory (DFT) has been critical towards our current atomistic understanding of catalysis on transition-metal surfaces. It has opened new paradigms in rational catalyst design, predicting fundamental properties, like the adsorption energy and reaction barriers, linked to catalytic performance. However, such applications depend sensitively on the predictive accuracy of DFT and achieving experimental-level reliability, so-called transition-metal chemical accuracy ( $13\text{ kJ mol}^{-1}$ ), remains challenging for present density functional approximations (DFAs) or even methods beyond DFT. We introduce a new framework for designing DFAs tailored towards studying molecules adsorbed on transition-metal surfaces, building upon recent developments in non-self-consistent DFAs. We propose two functionals within this framework, demonstrating that transition-metal chemical accuracy can be achieved across a diverse set of 39 adsorption reactions while delivering consistent performance for 17 barrier heights. Moreover, we show that these non-self-consistent DFAs address qualitative failures that challenge current self-consistent DFAs, such as CO adsorption on Pt(111) and graphene on Ni(111). The resulting functionals are computationally practical and compatible with existing DFT codes, with scripts and workflows provided to use them. Looking ahead, this framework establishes a path toward developing more accurate and sophisticated DFAs for computational heterogeneous catalysis and beyond.

## INTRODUCTION

Our atomic-level understanding of catalytic reactions on transition metal surfaces has greatly advanced in recent years thanks to density functional theory (DFT) [1]. Complex catalytic processes can be studied through kinetic models derived from barrier heights and adsorption energies computed from DFT [2, 3]. More generally, DFT has revealed the fundamental scaling relationships between properties such as the adsorption energy on a surface and its catalytic activity or selectivity [4–6]. With this framework, the complexity of heterogeneous catalysis can be simplified into easy-to-compute quantities, opening avenues for rational design [7]. For such applications, the effectiveness of DFT lies in an accurate determination of these central quantities [8, 9], and inaccurate prediction [10, 11] can readily mislabel a promising catalyst as an inert one or vice versa.

The practical application of DFT requires density functional approximations [12] (DFAs),

which span increasing sophistication from the local density approximation to generalized-gradient approximations (GGAs), meta-GGAs, hybrids, and double hybrids [13]. Although semilocal DFAs such as GGAs and meta-GGAs are the workhorse of computational materials science, they exhibit systematic failures for adsorption on transition metal surfaces [14]. For example, achieving errors below 20 kJ/mol across broad adsorption energy datasets has proved difficult [15], despite the fact that errors below 4 kJ/mol are attainable for insulator surfaces [16, 17]. Beyond quantitative errors, semilocal DFAs also fail to qualitatively describe the adsorption mechanism of molecules, most famously the CO adsorption puzzle [18]: across important transition-metal surfaces, semilocal DFAs consistently predict the wrong adsorption site for CO, incorrectly favoring the hollow (FCC) site over the (on-)top site.

The next level above semilocal DFAs are hybrid DFAs, which incorporate a fraction of exact exchange (EXX), and while their significantly higher cost is justified by clear improvements for insulators, the benefits for transition-metal surfaces are not clear. For example, the popular HSE06 DFA, a screened (range-separated) hybrid, has been applied to several transition metal surface datasets, where its accuracy for both adsorption energies [15] and barrier heights [19] is found to be worse than semilocal DFAs. Similarly, HSE06 and other common hybrid DFAs such as PBE0 and B3LYP show mixed success for the CO adsorption puzzle: while they perform well for some transition-metal surfaces [Cu(111) and Rh(111)], the canonical case of Pt(111) remains a persistent challenge [20]. By contrast, embedded cluster studies [21] have shown that the hybrid M06 can be applied to small clusters to locally correct PBE+D3 estimates from periodic slabs, reporting some of the most accurate predictions to date. However, the transferability of these approaches to global properties [22] (e.g., surface energies or monolayer adsorption) remains unclear. More fundamentally, the direct use of unscreened hybrid functionals to periodic metal slabs is questionable, due to their incorrect description of the band structure and their convergence challenges in the self-consistent field (SCF) cycle [23, 24].

Double hybrids represent the highest level of the DFA hierarchy, and these include information from unoccupied orbitals by incorporating a fraction of the correlation energy from second-order Møller-Plesset perturbation theory (MP2) or the random-phase approximation (RPA). The application of MP2-based double hybrids to periodic transition metal surfaces has been limited by their substantially increased cost and the formal divergence of the MP2 correlation energy for metallic systems [25, 26]. Such limitations can be sidestepped again via an embedded cluster, which has demonstrated success of the XYG3 DFA for adsorption on Cu surfaces [27]. In

contrast, RPA is well-defined for metals, which has allowed its widespread, direct application to periodic calculations in both its conventional and double-hybrid formulations [14, 24, 28–32]. While successful for selected systems, broader applications have revealed limitations in its accuracy [30, 33], motivating recent efforts [24, 34, 35] to empirically optimize RPA for improved performance across diverse systems.

In recent years, there have been significant developments in non-self-consistent (NSC) DFAs [36], in which orbitals and densities are obtained self-consistently with one functional and the energy is evaluated in a one-shot manner using another. This approach has been successful for molecular systems [37], where the meta-GGA SCAN [38] functional evaluated with Hartree-Fock orbitals (SCAN@HF) has shown strong performance for noncovalent interactions [39, 40] and reaction barriers [41]. More recently, this accuracy has also been demonstrated for solid transition-metal oxides by combining hybrid variants of  $r^2$ SCAN with separate exchange admixtures ( $r^2$ SCANX@ $r^2$ SCANY) [42]. NSC-DFAs have been less studied for surfaces, particularly transition metals, although one notable example is the dissociation of O<sub>2</sub> on Al(111), where HSE03-1/3x@RPBE was used to reproduce (self-consistent) HSE03-1/3x at lower costs [43, 44].

In this work, we introduce two new NSC-DFAs tailored for transition-metal surface chemistry. We start from a self-consistent calculation using the BEEF-vdW [45] DFA, which is a dispersion-corrected GGA that was designed for surface science and already exhibits good performance. From the BEEF-vdW orbitals, we construct a hybrid functional evaluated non-self-consistently (hBEEF-vdW@BEEF-vdW) with one additional free parameter for the fraction of exact exchange replacing semilocal exchange. We also construct a double-hybrid extension (dhBEEF-vdW@BEEF-vdW) with a second free parameter for the fraction of RPA correlation replacing semilocal correlation (see Methods). The new parameters of these NSC-DFAs are empirically tuned against a carefully curated, diverse dataset of seven accurate adsorption energies (Supplementary Section 2), but we show that their predictions are qualitatively and quantitatively accurate across a broad range of molecule-surface phenomena that were not used for tuning. Our hybrid DFA, hBEEF-vdW@BEEF-vdW, achieves accuracy comparable to that of RPA on a dataset of 39 adsorption energies while improving upon RPA on a dataset of 17 surface chemistry barrier heights. Notably, it resolves the CO adsorption puzzle, correctly predicting the preferred binding configuration of CO on Pt(111) that has challenged previous hybrids. Our double-hybrid DFA, dhBEEF-vdW@BEEF-vdW, yields substantial accuracy improvements over RPA, achieving

a mean absolute deviation of 11 kJ/mol (within “transition-metal chemical accuracy” [46] of 13 kJ mol<sup>-1</sup>) for adsorption energies and outperforming RPA for barrier heights, while retaining correct behavior for CO adsorption.

Both NSC-DFAs we propose are practical, cost-efficient, and compatible with existing DFT codes. We provide easy-to-modify recipes for the QuAcc automated workflow library [47], enabling immediate application to systems of interest. Beyond improved accuracy, they offer key advantages over their self-consistent counterparts. In particular, both DFAs avoid a hybrid SCF, which significantly lowers cost and precludes convergence issues. Our first DFA, hBEEF-vdW@BEEF-vdW, requires the equivalent of only one SCF cycle of a hybrid DFA, which is about 20 times more expensive than the GGA SCF calculation (Supplementary Table 1). Our second DFA, dhBEEF-vdW@BEEF-vdW, is designed to be only twice as expensive than hBEEF-vdW@BEEF-vdW by exploiting error cancelation (Methods) and leveraging the fact that the small fraction of RPA correlation (15%) allows less stringent convergence settings for adsorption energies. More broadly, this formalism opens a new avenue for DFA development for transition-metal surfaces, long dominated by GGAs and meta-GGAs, with substantial flexibility for further improvement.

## RESULTS

### Accurate adsorption energy predictions

We first validate our proposed NSC-DFAs against the CE39 dataset by Wellendorff *et al.* [48], which consists of experimental adsorption energies for 39 diverse reactions corrected for zero-point vibrational effects. It covers chemisorption and physisorption of key catalytic reactants such as hydrogen, alkanes, alcohols, water and oxygen on technologically-relevant transition-metal surfaces, and spans a large energy range of over 200 kJ mol<sup>-1</sup> per product. This dataset is a standard benchmark for computational catalysis and it has been a prevailing challenge [15, 49] to design DFAs that (1) achieve errors below 20 kJ mol<sup>-1</sup>, let alone the 13 kJ mol<sup>-1</sup> target that defines transition-metal chemical accuracy, and (2) give a balanced description of both physisorption and chemisorption.

We benchmark the performance of hBEEF-vdW@BEEF-vdW and dhBEEF-vdW@BEEF-vdW on the CE39 dataset against several common (self-consistent) DFAs and the RPA in Figure 1;

## CE39 adsorption energies on transition metal surfaces

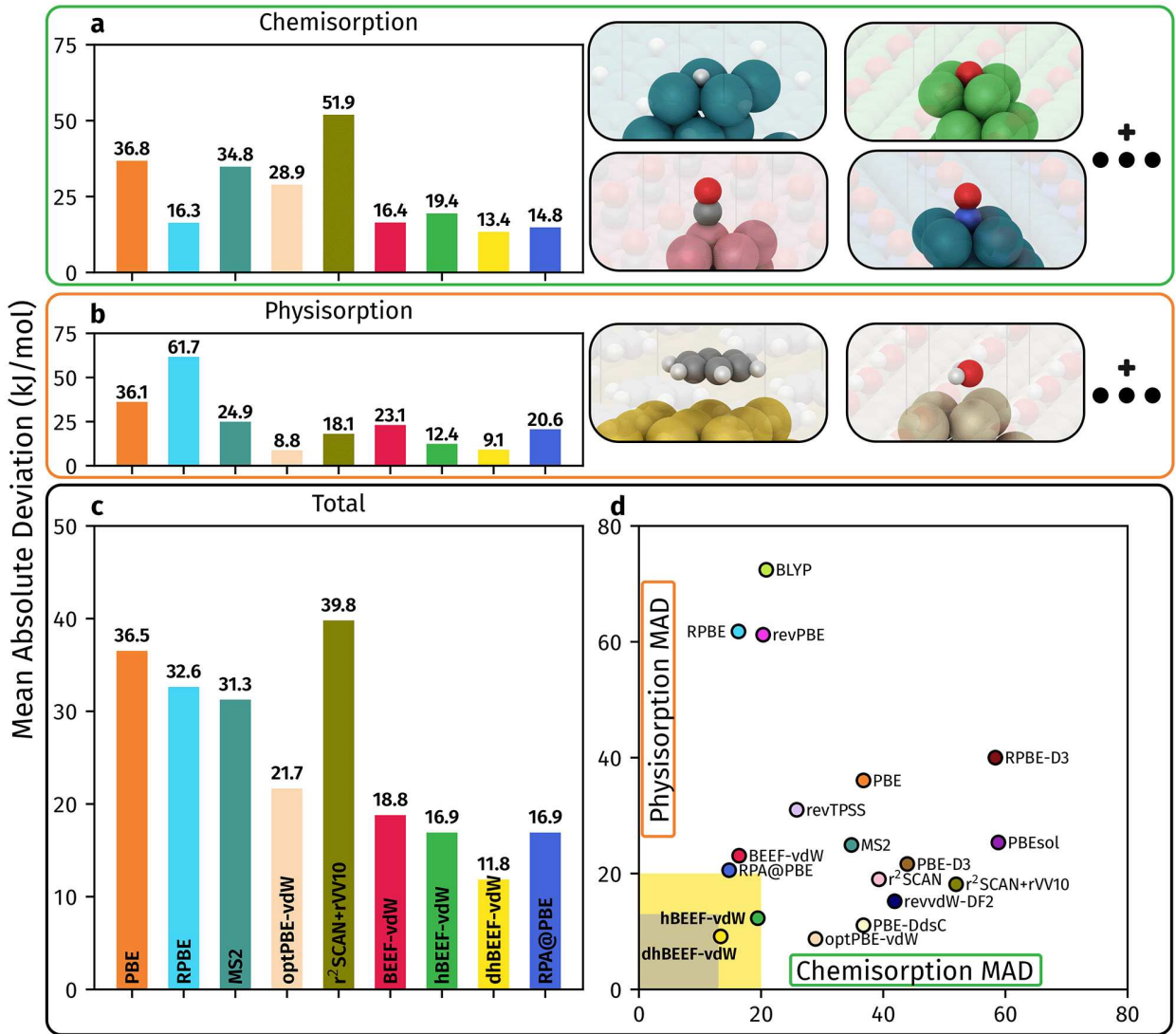


**Figure 1: Accurate and balanced performance for adsorption on transition metal surfaces.** Comparison of hBEEF-vdW@BEEF-vdW and dhBEEF-vdW@BEEF-vdW against common (self-consistent) density functional approximations for the adsorption energies of the CE39 dataset [48]. We give mean absolute deviations (per product formed) w.r.t. experimental values from Ref. 48 for the (a) chemisorption and (b) physisorption subsets. We also compare the (c) total performance and (d) show the correlation between the physisorption and chemisorption subset MADs.

here and throughout, we evaluate RPA with PBE orbitals (RPA@PBE), which is the most common choice in the literature. With the double-hybrid dhBEEF-vdW@BEEF-vdW, we obtain the best accuracy to date for the full CE39 dataset, leading to a mean absolute deviation (MAD)

of  $11.8 \text{ kJ/mol}$ , surpassing transition-metal chemical accuracy. Unlike many other DFAs and the RPA, the accuracy of dhBEEF-vdW@BEEF-vdW is also well-balanced, with an MAD of  $13.4 \text{ kJ mol}^{-1}$  and  $9.1 \text{ kJ mol}^{-1}$  on the chemisorbed and physisorbed subsets, respectively. The overall performance is about  $5 \text{ kJ mol}^{-1}$  more accurate than RPA, primarily due to a significant reduction of error on the physisorbed subset of the CE39 dataset, for which RPA has a MAD of  $20.6 \text{ kJ mol}^{-1}$ . Our hybrid hBEEF-vdW@BEEF-vdW improves upon the base BEEF-vdW DFA, bringing the MAD down from  $18.8 \text{ kJ mol}^{-1}$  to  $16.9 \text{ kJ mol}^{-1}$ , such that it rivals RPA at lower costs.

As shown in Figure 1d, we have benchmarked a broad set of DFAs and the RPA on the CE39 dataset and none has been able to reach errors below  $20 \text{ kJ mol}^{-1}$  on the chemisorption and physisorption subsets simultaneously (RPA and BEEF-vdW are the closest). Both hBEEF-vdW@BEEF-vdW and dhBEEF-vdW@BEEF-vdW achieve this goal, with dhBEEF-vdW@BEEF-vdW being the first DFA to achieve close to transition-metal chemical accuracy of  $13 \text{ kJ mol}^{-1}$  or better across both subsets of the CE39 dataset. The DFAs we benchmark are all widely employed in computational catalysis, and dhBEEF-vdW@BEEF-vdW represents the best performing for the chemisorption subset while rivaling the best performing DFA (optPBE-vdW at  $8.8 \text{ kJ mol}^{-1}$ ) for the physisorption subset, with hBEEF-vdW@BEEF-vdW also performing strongly at slightly lower cost.

### Reliable description of CO and graphene adsorption

Beyond quantitative improvements, our proposed NSC-DFAs also give qualitative improvements over standard self-consistent DFAs. As mentioned in the Introduction, predicting the correct CO adsorption site, particularly on Pt(111), has represented the canonical puzzle that has challenged GGAs, meta-GGAs and hybrid DFAs [20]. Similarly, the adsorption of graphene on Ni(111) has also been contentious [50, 51], due to a delicate competition between physisorption far from the surface and chemisorption close to the surface.

We compare a set of DFAs to our NSC-DFAs for CO adsorption across three transition metals [Pt(111), Rh(111) and Cu(111)] in Figure 2a, where the relative energy between the (on-)top and hollow (FCC) sites is plotted. Experimental measurements show that CO adsorbs on the top site for all three systems [52–54], but for both Cu(111) and Pt(111), the semilocal DFAs [r<sup>2</sup>SCAN-rVV10, PBE and BEEF-vdW] predict the hollow site to be most stable. For Cu(111),

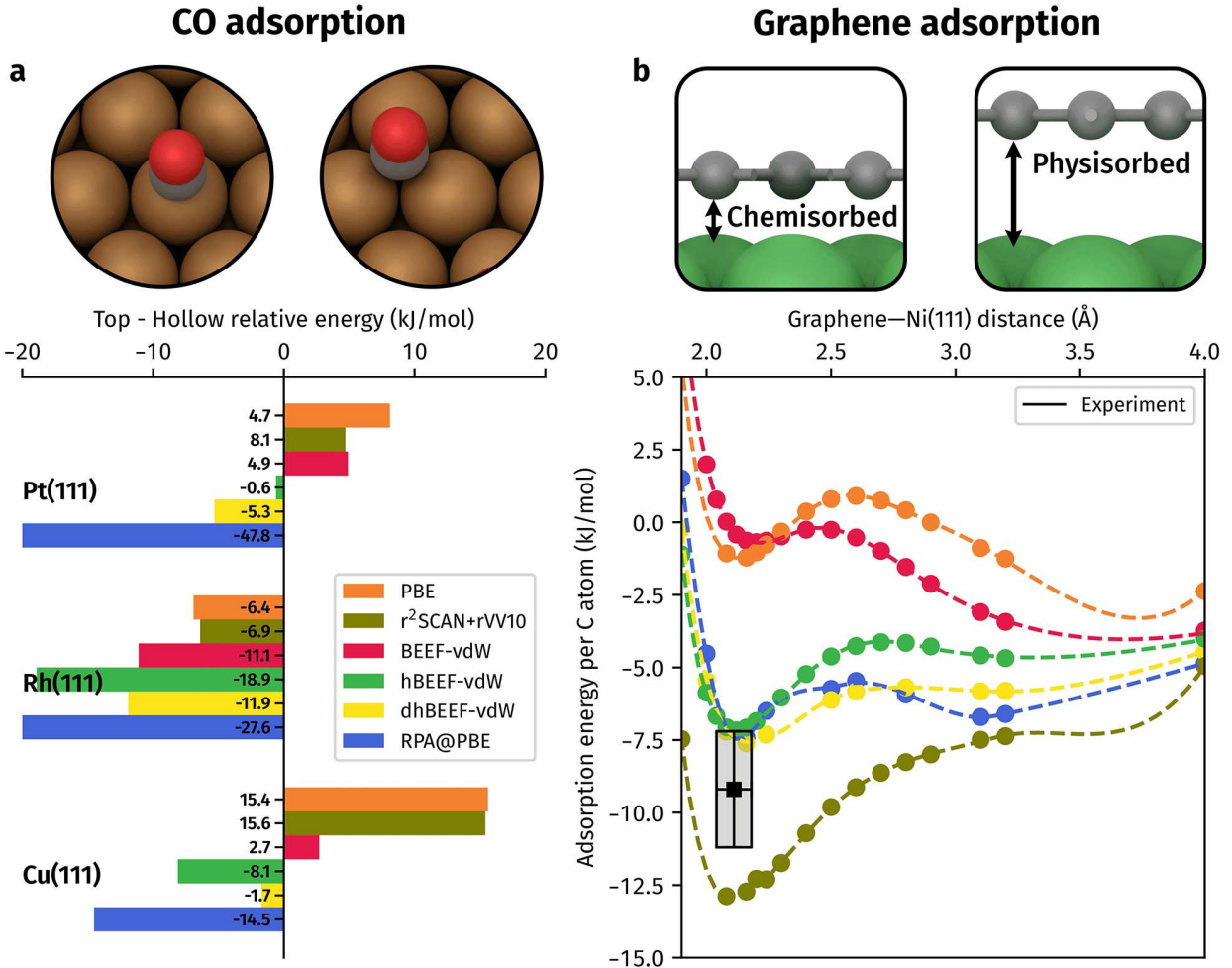


**Figure 2: Overcoming qualitative failures of self-consistent DFAs for adsorption.** Comparison of hBEEF-vdW@BEEF-vdW and dhBEEF-vdW@BEEF-vdW against common (self-consistent) density functional approximations for (a) CO adsorption on Pt(111), Rh(111) and Cu(111) and (b) graphene adsorption on Ni(111). We give the relative energy between the (on-)top and hollow (fcc) site in (a), with a negative value favoring the top site. The experimental value for the adsorption energy and distance in (b) were taken from Ref. 50.

the correct ordering is recovered with hBEEF-vdW@BEEF-vdW, which predicts a relative energy of  $-8.1 \text{ kJ mol}^{-1}$ , favoring the top site, whereas BEEF-vdW predicts  $+2.7 \text{ kJ mol}^{-1}$ . For Pt(111), hBEEF-vdW@BEEF-vdW also favors the top site, but only by  $-0.6 \text{ kJ mol}^{-1}$ . The top site is further favored when increasing the percentage of exact exchange (currently 17.5%) to higher levels (Supplementary Section 3A). The correct behavior is also observed from dhBEEF-vdW@BEEF-vdW, in part due to its higher fraction of exact exchange (the standard 25%). All

DFAs (including NSC-DFAs) are found to predict CO adsorption on Rh(111) correctly. The RPA consistently favors the top site quite strongly (by 15 to 48  $\text{kJ mol}^{-1}$ ) for all three transition-metal surfaces.

We compare the same set of DFAs for the adsorption of graphene on the Ni(111) surface in Figure 2b. Experiments indicate that it forms a chemisorbed state with an adsorption energy per C atom of  $-9.2 \pm 2.0 \text{ kJ mol}^{-1}$  and distance of  $2.11 \pm 0.11 \text{ pm}$  [50], highlighted in the gray box. PBE and BEEF-vdW fail to reproduce this result, predicting weak chemisorption stability and favoring the physisorbed configuration. In contrast, hBEEF-vdW@BEEF-vdW and dhBEEF-vdW@BEEF-vdW (and the RPA) predict the chemisorbed state to be the most stable, with an adsorption energy and chemisorption distance that lie within the errors bars of the experimental values.

### Towards right answers for the right reasons on surface barrier heights

We now assess the performance of our NSC-DFAs for reaction barrier heights on transition-metal surfaces, using the 17 reaction barriers compiled in the SBH17 dataset [55]. This dataset covers the dissociation of  $\text{CH}_4$ ,  $\text{H}_2$  and  $\text{N}_2$  on various surfaces of Ni, Cu, Ru, Ag, Ir, and Pt. In particular,  $\text{N}_2$  dissociation on Ru(0001) and Ru(10 $\bar{1}$ 0) consists of significant charge transfer, making them challenging barriers to predict. These reactions have been extensively studied, yet a persistent paradox is that PBE performs best for barrier heights despite being among the worst for adsorption energies (as we showed in Figure 1).

Figure 3a compares the performance of hBEEF-vdW@BEEF-vdW and dhBEEF-vdW@BEEF-vdW against several DFAs for the SBH17 dataset. While BEEF-vdW performs strongly for the CE39 dataset, its performance for the SBH17 dataset is weaker, with an MAD of 21.4  $\text{kJ mol}^{-1}$ . Both hBEEF-vdW@BEEF-vdW and dhBEEF-vdW@BEEF-vdW improve over BEEF-vdW, reaching an MAD of 17.4  $\text{kJ mol}^{-1}$  and 16.5  $\text{kJ mol}^{-1}$ , respectively. PBE remains the best, with an MAD of 11.6  $\text{kJ mol}^{-1}$  but its performance for the  $\text{N}_2$  dissociation subset is poor, giving an MAD of 53.5  $\text{kJ mol}^{-1}$ . These large errors are expected for systems with significant charge transfer but are masked in the SBH17 dataset, which includes only two  $\text{N}_2$  dissociation reactions, previously noted as a qualitative limitation of the dataset [32]. In fact, this failure is also inherited and exacerbated in RPA@PBE, leading to an MAD of 84.7  $\text{kJ mol}^{-1}$  for the  $\text{N}_2$  dissociation subset. Our two new DFAs, hBEEF-vdW@BEEF-vdW and dhBEEF-vdW@BEEF-vdW, give relatively

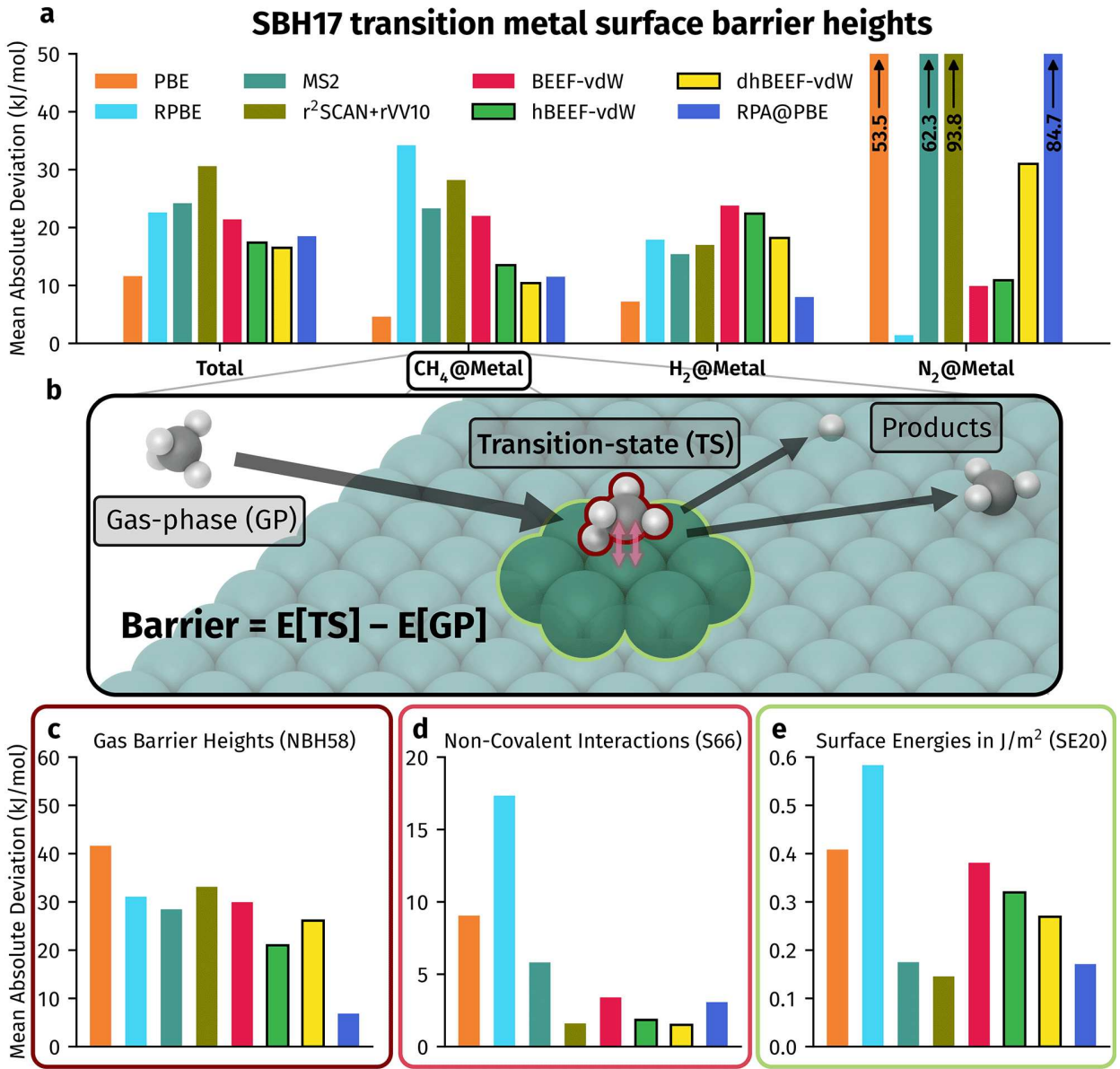


**Figure 3: Improved barrier heights for the right reasons on transition metal surfaces.** Comparison of hBEEF-vdW@BEEF-vdW and dhBEEF-vdW@BEEF-vdW against common (self-consistent) density functional approximations for the (a) SBH17 dataset [55]. We provide mean absolute deviations (MADs) against experimental values for the total SBH17 dataset as well as its CH<sub>4</sub> [visualized in (b)], H<sub>2</sub> and N<sub>2</sub> dissociation subsets. Further comparison is given for (c) gas-phase barrier heights (NBH58; the neutral subset of the BH46 and DBH22 datasets in Ref. 56), (d) gas-phase dimer non-covalent interactions (S66 dataset [57]) and (e) metal surface energies (SE20 dataset) from Ref. 58.

consistent performance across all three sets of systems, with the large errors from RPA for N<sub>2</sub> dissociation partially mitigated within dhBEEF-vdW@BEEF-vdW.

Improving barrier heights for the right reasons requires accurately describing all relevant components: (1) the gas-phase reaction barrier, (2) interactions between the transition state and the metal surface, and (3) surface restructuring. In Figures 3b-d, we assess the DFAs across these various components using the neutral subset of the DBH22 and BH46 gas-phase dataset of barrier heights [56] for (1), the S66 dataset [57] of dimer binding energies for (2), and the SE20 dataset [58] of metal surface energies for (3). For all of these datasets, PBE is one of the worst performing, suggesting that its good performance for CH<sub>4</sub> and H<sub>2</sub> barrier heights on metal surfaces arises from fortuitous error cancellation. On the other hand, hBEEF-vdW@BEEF-vdW and dhBEEF-vdW@BEEF-vdW are much better than PBE and consistently improve upon BEEF-vdW across all three datasets. There is still significant room for improvement, particularly for surface energies, where both hBEEF-vdW@BEEF-vdW and dhBEEF-vdW@BEEF-vdW perform worse than the r<sup>2</sup>SCAN-rVV10 DFA or the RPA. Additionally, RPA performs much better than the NSC-DFAs for reaction barriers, although this has been attributed to error cancellation [59].

## DISCUSSION

We discuss here the origins of the qualitative success of hBEEF-vdW@BEEF-vdW for the CO adsorption puzzle, particularly on Pt(111). Although self-consistent hybrid DFAs correct semilocal DFAs for Rh(111) and Cu(111), a comprehensive analysis of previous studies [20] showed that the issue persists for Pt(111), concluding that they “hardly improve the description of CO adsorption on metal surfaces.” As discussed in Supplementary Section 3, this reflects two competing effects: bonding to the hollow site is weakened due to a raised CO 2 $\pi^*$  level that suppresses electron back-donation from the metal, but its bonding is strengthened by the reduced steric repulsion as hybrids localize charge on metal atoms. As hBEEF-vdW@BEEF-vdW builds on top of the GGA BEEF-vdW density, the decreased steric repulsion does not occur. On the other hand, we show in Supplementary Section 3 that the 2 $\pi^*$  level continues to be raised. In fact, it increases as a function of the admixture of exact exchange, leading to a corresponding monotonic increase in the stability of the top site.

We now discuss the cost of both hBEEF-vdW@BEEF-vdW and dhBEEF-vdW@BEEF-vdW. Besides its qualitative and quantitative improvements, hBEEF-vdW@BEEF-vdW has a signifi-

cantly lower cost relative to self-consistent hybrid DFAs. As it builds on top of the GGA orbitals, the expensive cost of the EXX evaluation is limited to a single SCF cycle, in comparison to the tens to hundreds of SCF cycles that may be required for a self-consistent hybrid DFA. This leads to affordable computational costs of 900 CPU core-hours (CPUh) on average for each system in the CE39 dataset. On top of the single EXX evaluation, dhBEEF-vdW@BEEF-vdW requires the additional cost to evaluate RPA correlation energy. Although RPA is traditionally more expensive than self-consistent hybrid DFAs [33], we have taken several practical measures (detailed in the Methods) to ensure that it is on average only twice the cost of a single EXX evaluation (i.e., the cost of hBEEF-vdW@BEEF-vdW), making it significantly cheaper to evaluate than self-consistent hybrids. Briefly, (1) the preceding BEEF-vdW results can be reused to overcome finite-size effects and (2) relaxed electronic-structure settings can be used for the RPA correlation energy as it is scaled to only 15% in dhBEEF-vdW@BEEF-vdW.

This work highlights that significant improvements can be obtained from only 1 or 2 universal parameters in hBEEF-vdW@BEEF-vdW and dhBEEF-vdW@BEEF-vdW, respectively. We adopt simple corrections, adding fixed fractions of exact exchange or RPA correlation to GGA orbitals and densities. This makes the approach practical and cost-effective to implement in existing DFT codes (see Supplementary Section 1). However, this choice also limits the level of accuracy that can be achieved. Notably, the performance on gas-phase datasets in Figure 3 is still lacking when compared to modern empirically-parametrized hybrid DFAs. Our proposed non-self-consistent DFA framework allows flexibility in both the hybrid DFA energy evaluation and the GGA used to generate the density, offering opportunities for further improvement by modifying either choice. Furthermore, previous work [24, 35, 60] has shown that relaxing physical constraints in RPA, by scaling correlation beyond unity, can improve accuracy across diverse systems; this strategy can be extended within the present framework for our NSC double-hybrid DFA.

## CONCLUSIONS

In summary, we introduce a framework for generating improved density functional approximations to study adsorption on metallic surfaces, where a hybrid or double-hybrid DFA is evaluated non-self-consistently on GGA densities. We have proposed two DFAs within this framework: the hybrid hBEEF-vdW@BEEF-vdW and the double-hybrid dhBEEF-vdW@BEEF-vdW. We show that hBEEF-vdW@BEEF-vdW resolves qualitative challenges within standard self-consistent hy-

brid density functionals, predicting the correct CO adsorption site on Pt(111) while providing improved adsorption energies and reaction barriers over BEEF-vdW, considered the current workhorse method for metallic surfaces. We find that dhBEEF-vdW@BEEF-vdW can achieve transition metal chemical accuracy on this large dataset of adsorption energies, together with a further improvement in reaction barriers. These improvements to the reaction barriers on transition metal surfaces are demonstrated to be for the right reasons, yielding better gas-phase barrier heights, non-covalent interactions, and surface energies. The framework has been implemented as an easy-to-use recipe in the QuAcc computational workflow library [47], enabling high-throughput calculations across diverse metal surfaces. We anticipate that these functionals will provide improved and reliable descriptions of metal surfaces at practical cost, with ample scope for further development within this framework.

## METHODS

### Non-self-consistent density functional approximations for metals

We describe our two non-self-consistent (NSC) density functional approximations (DFAs) in this section. This is a general framework where the density is evaluated with one functional, while the energy is evaluated with a different functional. This framework is motivated by the partitioning of DFT errors into functional-driven and density-driven contributions: different DFAs may be better at address one or the other, or enable error cancellation between them [61]. In molecules and insulators, these errors can be empirically reduced [36, 61] by using Hartree-Fock or high-exact-exchange hybrids for the density and SCAN-like meta-GGAs for the energy. In this work, we adapt the framework to metals by using semilocal DFAs (e.g., BEEF-vdW) to generate densities and evaluating hybrid or double-hybrid functionals non-self-consistently. Owing to the delocalized character of metals, GGAs such as BEEF-vdW are expected to produce more reliable densities [45, 62, 63] than hybrids, while hybrid or double-hybrid evaluations on these densities address functional-driven errors.

For our hybrid NSC-DFA, we use the exchange (BF<sub>x</sub>) and correlation (BF<sub>c</sub>) functionals from BEEF-vdW (BF-vdW) in the form:

$$E_{xc}^{\text{hBF-vdW}} = a_h \cdot E_x^{\text{HF}}[n^{\text{BF-vdW}}] + (1 - a_h) \cdot E_x^{\text{BFx}}[n^{\text{BF-vdW}}] + E_c^{\text{BFc}}[n^{\text{BF-vdW}}] + E_c^{\text{NL}}[n^{\text{BF-vdW}}], \quad (1)$$

where  $n^{\text{BF-vdW}}$  is the (self-consistent) electron density from BF-vdW, with the parameter  $a_h$  being

the fraction of the Hartree-Fock (HF) mixed with BF<sub>x</sub>, while  $E_c^{\text{NL}}$  is the non-local van der Waals correlation contribution. As shown in Supplementary Section 2, we find that an  $a_h$  value of 0.175 to be optimal for a small set of 7 adsorption energies taken from the CE39 dataset.

For our double-hybrid NSC-DFA, we also mix in a fraction of RPA correlation (RPAc) energy. The RPAc was evaluated on PBE orbitals as we show in Supplementary Section 2B that it gave significant improvements over BEEF-vdW orbitals:

$$E_{\text{xc}}^{\text{dhBF-vdW}} = a_{dh} \cdot E_x^{\text{HF}}[n^{\text{BF-vdW}}] + (1 - a_{dh}) \cdot E_x^{\text{BFx}}[n^{\text{BF-vdW}}] + b_{dh} \cdot E_c^{\text{RPAc}}[n^{\text{PBE}}] + (1 - b_{dh}) \cdot E_c^{\text{BFc}}[n^{\text{BF-vdW}}] + E_c^{\text{NL}}[n^{\text{BF-vdW}}], \quad (2)$$

where  $a_{dh} = 0.25$  and  $b_{dh} = 0.15$  are the fractions of exact exchange and RPA correlation chosen based upon an optimization on the same set of 7 adsorption energies.

### Modeling procedure for adsorption energy and barrier heights

All our adsorption energy calculations were modeled with 4 layer (L) slabs with a subsequent correction towards a larger number (5 or 6) of layers. The adsorption energy for DFT calculations have the form:

$$E_{\text{ads}} = E[\text{Mol@Slab}] - E[\text{Mol}] - E[\text{Slab}] + \Delta E_{\text{ads}}^{\text{layer}}. \quad (3)$$

Here,  $E[\text{Mol}]$ ,  $E[\text{Slab}]$  and  $E[\text{Mol@Slab}]$  are the total electronic energies of the molecule (Mol), surface slab and the adsorbed complex, respectively. The molecule calculations were performed in a large unit cell box with 15 Å of vacuum in each direction. The  $\Delta E_{\text{ads}}^{\text{layer}}$  accounts for the finite-size errors of the 4L slab with respect to an infinite layer slab and is obtained by subtracting the adsorption energy for the 4L slab from the 6L slab using BEEF-vdW. For the RPA calculations, we took a slightly different approach, where:

$$E_{\text{ads}} = E[\text{Mol@Slab}] - E[\text{Mol//Slab}] - E[\text{Slab}] - \Delta E_{\text{lat}}^{\text{DFT}} + \Delta E_{\text{ads}}^{\text{layer}}. \quad (4)$$

Here, the molecule is placed in the same unit cell (uc) as the slab or adsorbed complex together with the same  $k$ -point mesh. This choice incorporates lateral interactions, but making convergence of properties such as the basis-set (i.e., energy cutoff) and integration grids cheaper for the RPA component. The lateral interactions are removed by calculating its contribution at the BF-vdW level in the  $\Delta E_{\text{lat}}^{\text{DFT}}$  term.

The geometries for the SBH17 dataset were taken from Ref. 55, which were optimized using the PBE DFA, and already contain a sufficient number of layers. There are two structures for

each system: the molecule in the gas-phase placed more than 10 Å away from the slab (dubbed GP+Slab), and the adsorbed molecule in its transition-state on the slab (TS+Slab). For the DFT calculations, we calculated the barrier height as follows:

$$E_b = E[\text{TS+Slab}] - E[\text{GP+Slab}]. \quad (5)$$

The resulting unit cell (and thus number of plane-waves) is very large to accommodate vacuum around both the gas-phase molecule and the slab in GP+Slab. This can make the RPA and EXX calculations quite costly. For these contributions, we instead generated structures truncated down to 4 layers with a 15 Å vacuum (w.r.t. the slab) indicated by “4L,small”. The molecule (from the gas-phase geometry) is placed within same unit cell in a separate calculation.

$$E_b = E[\text{TS+Slab}_{4\text{L,small}}] - E[\text{Mol//GP+Slab}_{4\text{L,small}}] - E[\text{Slab}_{4\text{L,small}}]. \quad (6)$$

We find that barrier heights computed in Equation 6 closely approximated the original Equation 5 to less than 3 kJ mol<sup>-1</sup> on average across the SBH17 dataset.

### Density functional theory calculation details

Most DFT calculations presented in this work were performed in the Vienna *Ab Initio* Simulation Package (VASP) [64–66]. We used the standard projector augmented wave (PAW) potentials for the DFT calculations and the associated GW-optimized PAW potentials for the RPA calculations. For the Ir and Ru elements, smaller core GW-optimized PAW potentials were used for the RPA calculations due to unavailability for the standard valence core. The DFT calculations were performed with a 550 eV energy cutoff, and we used a  $9 \times 9 \times 1$  and  $6 \times 6 \times 1$   $k$ -point mesh for the  $2 \times 2$  and  $3 \times 3$  slabs within the CE39 dataset and CO adsorption calculations, respectively. This  $k$ -point mesh was increased to  $12 \times 12 \times 1$  and  $8 \times 8 \times 1$  for the HF and RPA components of the hybrid and double-hybrid calculations. We used a  $9 \times 9 \times 1$   $k$ -point mesh for all components for the SBH17 dataset and  $12 \times 12 \times 1$   $k$ -point mesh for the adsorption of graphene on Ni(111). The RPA calculations were performed with a smaller 310 eV cutoff and extrapolated to the basis set limit. The DFT calculations were performed with a smearing width of 0.10 eV and Methfessel-Paxton smearing. Both the HF and RPA calculations were performed with the same smearing width, but with Fermi-Dirac smearing, where we have used the finite-temperature formalism [67] of RPA. We used Normal fast Fourier transform (FFT) grids

for the exact-exchange routines for HF, while the Fast settings were used in evaluating the RPA correlation energy.

### Gas-phase random phase approximation calculation details

RPA calculations were performed in the MRCC [68] molecular quantum chemistry code for the gas-phase NBH58 and S66 datasets in Figure 3. The complete basis set limit was reached using a two point extrapolation [69] of the aug-cc-pVQZ and aug-cc-pV5Z pair of basis sets for the separate EXX and correlation energy components.

### DATA AVAILABILITY

All data required to reproduce the findings of this study will be made available upon publication of this study.

### ACKNOWLEDGMENTS

The Flatiron Institute is a division of the Simons Foundation.

---

\* [mail@benjaminshi.com](mailto:mail@benjaminshi.com)

\* [t.berkelbach@columbia.edu](mailto:t.berkelbach@columbia.edu)

- [1] J. K. Nørskov, T. Bligaard, J. Rossmeisl, and C. H. Christensen, Towards the computational design of solid catalysts, *Nat. Chem.* **1**, 37 (2009).
- [2] C. Jiang, B. Yan, B. R. Goldsmith, and S. Linic, Predictive model for the discovery of sinter-resistant supports for metallic nanoparticle catalysts by interpretable machine learning, *Nat. Catal.* **8**, 1038 (2025).
- [3] F. Lorenzutti, R. R. Seemakurthi, E. F. Johnson, S. Morandi, P. Nikačević, N. López, and S. Haussener, Microenvironment effects in electrochemical CO<sub>2</sub> reduction from first-principles multiscale modelling, *Nat. Catal.* **8**, 905 (2025).

[4] A. Michaelides, Z.-P. Liu, C. J. Zhang, A. Alavi, D. A. King, and P. Hu, Identification of general linear relationships between activation energies and enthalpy changes for dissociation reactions at surfaces, *J. Am. Chem. Soc.* **125**, 3704 (2003).

[5] T. Bligaard, J. K. Nørskov, S. Dahl, J. Matthiesen, C. H. Christensen, and J. Sehested, The Brønsted–Evans–Polanyi relation and the volcano curve in heterogeneous catalysis, *J. Catal.* **224**, 206 (2004).

[6] Q. Wang, S.-F. Hung, K. Lao, X. Huang, F. Li, H. B. Tao, H. B. Yang, W. Liu, W. Wang, Y. Cheng, N. Hiraoka, L. Zhang, J. Zhang, Y. Liu, J. Chen, Y. Xu, C. Su, J. G. Chen, and B. Liu, Breaking the linear scaling limit in multi-electron-transfer electrocatalysis through intermediate spillover, *Nat. Catal.* **8**, 378 (2025).

[7] Z.-J. Zhao, S. Liu, S. Zha, D. Cheng, F. Studt, G. Henkelman, and J. Gong, Theory-guided design of catalytic materials using scaling relationships and reactivity descriptors, *Nat. Rev. Mater.* **4**, 792 (2019).

[8] F. Calle-Vallejo, J. Tymoczko, V. Colic, Q. H. Vu, M. D. Pohl, K. Morgenstern, D. Loffreda, P. Sautet, W. Schuhmann, and A. S. Bandarenka, Finding optimal surface sites on heterogeneous catalysts by counting nearest neighbors, *Science* **350**, 185 (2015).

[9] R. T. Hannagan, G. Giannakakis, R. Réocreux, J. Schumann, J. Finzel, Y. Wang, A. Michaelides, P. Deshlahra, P. Christopher, M. Flytzani-Stephanopoulos, M. Stamatakis, and E. C. H. Sykes, First-principles design of a single-atom–alloy propane dehydrogenation catalyst, *Science* **372**, 1444 (2021).

[10] G. Di Liberto, L. A. Cipriano, and G. Pacchioni, Universal principles for the rational design of single atom electrocatalysts? Handle with care, *ACS Catal.* **12**, 5846 (2022).

[11] H. Xu, D. Cheng, D. Cao, and X. C. Zeng, Revisiting the universal principle for the rational design of single-atom electrocatalysts, *Nat. Catal.* **7**, 207 (2024).

[12] J. P. Perdew and K. Schmidt, Jacob's ladder of density functional approximations for the exchange-correlation energy, *AIP Conf. Proc.* **577**, 1 (2001).

[13] L. Goerigk, A. Hansen, C. Bauer, S. Ehrlich, A. Najibi, and S. Grimme, A look at the density functional theory zoo with the advanced GMTKN55 database for general main group thermochemistry, kinetics and noncovalent interactions, *Phys. Chem. Chem. Phys.* **19**, 32184 (2017).

[14] L. Schimka, J. Harl, A. Stroppa, A. Grüneis, M. Marsman, F. Mittendorfer, and G. Kresse, Accurate surface and adsorption energies from many-body perturbation theory, *Nat. Mater.* **9**, 741 (2010).

[15] S. Mallikarjun Sharada, R. K. B. Karlsson, Y. Maimaiti, J. Voss, and T. Bligaard, Adsorption on transition metal surfaces: Transferability and accuracy of DFT using the ADS41 dataset, *Phys. Rev. B* **100**, 035439 (2019).

[16] F. R. Rehak, G. Piccini, M. Alessio, and J. Sauer, Including dispersion in density functional theory for adsorption on flat oxide surfaces, in metal–organic frameworks and in acidic zeolites, *Phys. Chem. Chem. Phys.* **22**, 7577 (2020).

[17] B. X. Shi, A. S. Rosen, T. Schäfer, A. Grüneis, V. Kapil, A. Zen, and A. Michaelides, An accurate and efficient framework for modelling the surface chemistry of ionic materials, *Nat. Chem.* **17**, 1688 (2025).

[18] P. J. Feibelman, B. Hammer, J. K. Nørskov, F. Wagner, M. Scheffler, R. Stumpf, R. Watwe, and J. Dumesic, The CO/Pt(111) puzzle, *J. Phys. Chem. B* **105**, 4018 (2001).

[19] S. Mallikarjun Sharada, T. Bligaard, A. C. Luntz, G.-J. Kroes, and J. K. Nørskov, SBH10: A benchmark database of barrier heights on transition metal surfaces, *J. Phys. Chem. C* **121**, 19807 (2017).

[20] A. Stroppa and G. Kresse, The shortcomings of semi-local and hybrid functionals: What we can learn from surface science studies, *New J. Phys.* **10**, 063020 (2008).

[21] R. B. Araujo, G. L. S. Rodrigues, E. C. dos Santos, and L. G. M. Pettersson, Adsorption energies on transition metal surfaces: Towards an accurate and balanced description, *Nat. Commun.* **13**, 6853 (2022).

[22] P. Janthon, S. A. Luo, S. M. Kozlov, F. Viñes, J. Limtrakul, D. G. Truhlar, and F. Illas, Bulk properties of transition metals: A challenge for the design of universal density functionals, *J. Chem. Theory Comput.* **10**, 3832 (2014).

[23] T. N. Mihm, T. Schäfer, S. K. Ramadugu, L. Weiler, A. Grüneis, and J. J. Shepherd, A shortcut to the thermodynamic limit for quantum many-body calculations of metals, *Nat. Comput. Sci.* **1**, 801 (2021).

[24] N.-K. Yu, J. Voss, and A. J. Medford, Optimization of random phase approximation calculations for improved energies of molecules, solids, and surfaces, *arXiv [physics.chem-phy]*, arXiv:2602.05138 (2026).

[25] E. Keller, T. Tsatsoulis, K. Reuter, and J. T. Margraf, Regularized second-order correlation methods for extended systems, *J. Chem. Phys.* **156**, 024106 (2022).

[26] K. Bystrom and T. C. Berkelbach, Size-consistent adiabatic connection functionals via orbital-based matrix interpolation, *J. Chem. Theory Comput.* **22**, 940 (2026).

[27] Z. Chen, Z. Liu, and X. Xu, Accurate descriptions of molecule-surface interactions in electrocatalytic CO<sub>2</sub> reduction on the copper surfaces, *Nat. Commun.* **14**, 936 (2023).

[28] T. Olsen and K. S. Thygesen, Random phase approximation applied to solids, molecules, and graphene-metal interfaces: From van der Waals to covalent bonding, *Phys. Rev. B* **87**, 075111 (2013).

[29] J. A. Garrido Torres, B. Ramberger, H. A. Früchtli, R. Schaub, and G. Kresse, Adsorption energies of benzene on close packed transition metal surfaces using the random phase approximation, *Phys. Rev. Mater.* **1**, 060803 (2017).

[30] P. S. Schmidt and K. S. Thygesen, Benchmark database of transition metal surface and adsorption energies from many-body perturbation theory, *J. Phys. Chem. C* **122**, 4381 (2018).

[31] C. Sheldon, J. Paier, and J. Sauer, Adsorption of CH<sub>4</sub> on the Pt(111) surface: Random phase approximation compared to density functional theory, *J. Chem. Phys.* **155**, 174702 (2021).

[32] B. Oudot and K. Doblhoff-Dier, Reaction barriers at metal surfaces computed using the random phase approximation: Can we beat DFT in the generalized gradient approximation?, *J. Chem. Phys.* **161**, 054708 (2024).

[33] N. A. Szaro, M. Bello, C. H. Fricke, O. H. Bamidele, and A. Heyden, Benchmarking the accuracy of density functional theory against the random phase approximation for the ethane dehydrogenation network on Pt(111), *J. Phys. Chem. Lett.* **14**, 10769 (2023).

[34] P. D. Mezei, G. I. Csonka, A. Ruzsinszky, and M. Kállay, Construction and application of a new dual-hybrid random phase approximation, *J. Chem. Theory Comput.* **11**, 4615 (2015).

[35] H. Kim, N.-K. Yu, N. Tian, and A. J. Medford, Assessing exchange-correlation functionals for heterogeneous catalysis of nitrogen species, *J. Phys. Chem. C* **128**, 11159 (2024).

[36] E. Sim, S. Song, S. Vuckovic, and K. Burke, Improving results by improving densities: Density-corrected density functional theory, *J. Am. Chem. Soc.* **144**, 6625 (2022).

[37] S. Song, S. Vuckovic, Y. Kim, H. Yu, E. Sim, and K. Burke, Extending density functional theory with near chemical accuracy beyond pure water, *Nat. Commun.* **14**, 799 (2023).

[38] J. Sun, A. Ruzsinszky, and J. P. Perdew, Strongly constrained and appropriately normed semilocal density functional, *Phys. Rev. Lett.* **115**, 036402 (2015).

[39] A. D. Kaplan, C. Shahi, R. K. Sah, P. Bhetwal, B. Kanungo, V. Gavini, and J. P. Perdew, How does HF-DFT achieve chemical accuracy for water clusters?, *J. Chem. Theory Comput.* **20**, 5517 (2024).

[40] Y. Kim, M. Sim, M. Lee, S. Kim, S. Song, K. Burke, and E. Sim, Extending density-corrected density functional theory to large molecular systems, *J. Phys. Chem. Lett.* **16**, 939 (2025).

[41] A. D. Kaplan, C. Shahi, P. Bhetwal, R. K. Sah, and J. P. Perdew, Understanding density-driven errors for reaction barrier heights, *J. Chem. Theory Comput.* **19**, 532 (2023).

[42] H. R. Gopidi, R. Zhang, Y. Wang, A. Patra, J. Sun, A. Ruzsinszky, J. P. Perdew, and P. Canepa, Reducing self-interaction error in transition-metal oxides with different exact-exchange fractions for energy and density, *arXiv [cond-mat.mtrl-sci]*, arXiv:2506.20635 (2025).

[43] N. Gerrits, E. W. F. Smeets, S. Vuckovic, A. D. Powell, K. Dobhoff-Dier, and G.-J. Kroes, Density functional theory for molecule–metal surface reactions: When does the generalized gradient approximation get it right, and what to do if it does not, *J. Phys. Chem. Lett.* **11**, 10552 (2020).

[44] R. A. B. van Bree, N. Gerrits, and G.-J. Kroes, Dissociative chemisorption of O<sub>2</sub> on Al(111): Dynamics on a potential energy surface computed with a non-self-consistent screened hybrid density functional approach, *Faraday Discuss.* **251**, 361 (2024).

[45] J. Wellendorff, K. T. Lundgaard, A. Møgelhøj, V. Petzold, D. D. Landis, J. K. Nørskov, T. Bligaard, and K. W. Jacobsen, Density functionals for surface science: Exchange-correlation model development with Bayesian error estimation, *Phys. Rev. B* **85**, 235149 (2012).

[46] N. J. DeYonker, K. A. Peterson, G. Steyl, A. K. Wilson, and T. R. Cundari, Quantitative computational thermochemistry of transition metal species, *J. Phys. Chem. A* **111**, 11269 (2007).

[47] A. S. Rosen, Quacc – The Quantum Accelerator: <https://zenodo.org/records/13921187>, Zenodo (2024).

[48] J. Wellendorff, T. L. Silbaugh, D. Garcia-Pintos, J. K. Nørskov, T. Bligaard, F. Studt, and C. T. Campbell, A benchmark database for adsorption bond energies to transition metal surfaces and comparison to selected DFT functionals, *Surf. Sci.* **640**, 36 (2015).

[49] M. Kothakonda, R. Zhang, J. Ning, J. Furness, A. Patra, Q. Zhao, and J. Sun, Towards chemical accuracy for chemi- and physisorption with an efficient density functional, *arXiv [cond-mat.mtrl-sci]*, arXiv:2410.11248 (2024).

[50] P. Janthon, F. Viñes, S. M. Kozlov, J. Limtrakul, and F. Illas, Theoretical assessment of graphene–metal contacts, *J. Chem. Phys.* **138**, 244701 (2013).

[51] M. S. Christian, A. Otero-de-la-Roza, and E. R. Johnson, Adsorption of graphene to nickel (111) using the exchange-hole dipole moment model, *Carbon* **118**, 184 (2017).

[52] B. E. Hayden, K. Kretzschmar, and A. M. Bradshaw, An infrared spectroscopic study of CO on Cu(111): The linear, bridging and physisorbed species, *Surf. Sci.* **155**, 553 (1985).

[53] D. F. Ogletree, M. A. Van Hove, and G. A. Somorjai, LEED intensity analysis of the structures of clean Pt(111) and of CO adsorbed on Pt(111) in the c(4 × 2) arrangement, *Surf. Sci.* **173**, 351 (1986).

[54] A. Beutler, E. Lundgren, R. Nyholm, J. N. Andersen, B. Setlik, and D. Heskett, On the adsorption sites for CO on the Rh(111) single crystal surface, *Surf. Sci.* **371**, 381 (1997).

[55] T. Tchakoua, N. Gerrits, E. W. F. Smeets, and G.-J. Kroes, SBH17: Benchmark database of barrier heights for dissociative chemisorption on transition metal surfaces, *J. Chem. Theory Comput.* **19**, 245 (2023).

[56] J. Liang and M. Head-Gordon, Gold-standard chemical database 137 (GSCDB137): A diverse set of accurate energy differences for assessing and developing density functionals, *J. Chem. Theory Comput.* **21**, 12601 (2025).

[57] J. Řezáč, K. E. Riley, and P. Hobza, S66: A well-balanced database of benchmark interaction energies relevant to biomolecular structures, *J. Chem. Theory Comput.* **7**, 2427 (2011).

[58] K. T. Lundgaard, J. Wellendorff, J. Voss, K. W. Jacobsen, and T. Bligaard, mBEEF-vdW: Robust fitting of error estimation density functionals, *Phys. Rev. B* **93**, 235162 (2016).

[59] T. Gould, A. Ruzsinszky, and J. P. Perdew, Simple self-interaction correction to random-phase-approximation-like correlation energies, *Phys. Rev. A* **100**, 022515 (2019).

[60] H. Jiang and E. Engel, Random-phase-approximation-based correlation energy functionals: Benchmark results for atoms, *J. Chem. Phys.* **127**, 184108 (2007).

[61] B. Kanungo, A. D. Kaplan, C. Shahi, V. Gavini, and J. P. Perdew, Unconventional error cancellation explains the success of Hartree-Fock density functional theory for barrier heights, *J. Phys. Chem. Lett.* **15**, 323 (2024).

[62] J. Paier, M. Marsman, and G. Kresse, Why does the B3LYP hybrid functional fail for metals?, *J. Chem. Phys.* **127**, 024103 (2007).

[63] W. Gao, T. A. Abtew, T. Cai, Y.-Y. Sun, S. Zhang, and P. Zhang, On the applicability of hybrid functionals for predicting fundamental properties of metals, *Solid State Commun.* **234–235**, 10 (2016).

- [64] G. Kresse and J. Furthmüller, Efficiency of ab-initio total energy calculations for metals and semiconductors using a plane-wave basis set, *Comput. Mater. Sci.* **6**, 15 (1996).
- [65] G. Kresse and J. Furthmüller, Efficient iterative schemes for ab initio total-energy calculations using a plane-wave basis set, *Phys. Rev. B* **54**, 11169 (1996).
- [66] G. Kresse and D. Joubert, From ultrasoft pseudopotentials to the projector augmented-wave method, *Phys. Rev. B* **59**, 1758 (1999).
- [67] M. Kaltak and G. Kresse, Minimax isometry method: A compressive sensing approach for Matsubara summation in many-body perturbation theory, *Phys. Rev. B* **101**, 205145 (2020).
- [68] M. Kállay, P. R. Nagy, D. Mester, Z. Rolik, G. Samu, J. Csontos, J. Csóka, P. B. Szabó, L. Gyevi-Nagy, B. Hégely, I. Ladjánszki, L. Szegedy, B. Ladóczki, K. Petrov, M. Farkas, P. D. Mezei, and Á. Ganyecz, The MRCC program system: Accurate quantum chemistry from water to proteins, *J. Chem. Phys.* **152**, 074107 (2020).
- [69] F. Neese and E. F. Valeev, Revisiting the atomic natural orbital approach for basis sets: Robust systematic basis sets for explicitly correlated and conventional correlated ab initio methods?, *J. Chem. Theory Comput.* **7**, 33 (2011).

# Supplementary Information: Practical and improved density functionals for computational catalysis on metal surfaces

Benjamin X. Shi<sup>1,\*</sup> and Timothy C. Berkelbach<sup>1,2,\*</sup>

<sup>1</sup>*Initiative for Computational Catalysis,*

*Flatiron Institute, New York, NY 10010, USA*

<sup>2</sup>*Department of Chemistry, Columbia University, New York, NY 10027, USA*

(Dated: February 17, 2026)

## CONTENTS

1. Performing hBEEF-vdW@BEEF-vdW and dhBEEF-vdW@BEEF-vdW	2
2. Optimizing the hBEEF-vdW and dhBEEF-vdW coefficients	6
A. Effect of HF screening parameter	7
B. PBE vs. BEEF-vdW orbitals for RPA correlation	12
3. Qualitative improvements on CO adsorption puzzle	14
A. Effect of exact exchange	14
B. Changes in the density of states for CO on Pt(111)	15
4. Timing ratios between RPA, EXX and DFT	16
References	16

---

\* [mail@benjaminshi.com](mailto:mail@benjaminshi.com)

\* [t.berkelbach@columbia.edu](mailto:t.berkelbach@columbia.edu)

## 1. PERFORMING HBEEF-VDW@BEEF-VDW AND DHBEEF-VDW@BEEF-VDW

Performing calculations of either hBEEF-vdW@BEEF-vdW and dhBEEF-vdW@BEEF-vdW requires VASP interfaced to the LIBXC library [1] of exchange-correlation and kinetic energy functionals. Both hBEEF-vdW@BEEF-vdW and dhBEEF-vdW@BEEF-vdW follow the same set of calculations, with dhBEEF-vdW@BEEF-vdW incorporating a subsequent set of RPA calculations. This results in 4 calculations for hBEEF-vdW@BEEF-vdW and 7 calculations for dhBEEF-vdW@BEEF-vdW (or 8 if the total RPA energy is wanted). This may seem like a lot of calculations but within the Github data repository (to be shared upon publication), we provide bash scripts to automate the entire process in VASP. Furthermore, we also provide a pre-built recipe for the QuAcc computational workflow library that will allow for automated high-throughput calculations with hBEEF-vdW@BEEF-vdW or dhBEEF-vdW@BEEF-vdW.

The set of calculations for hBEEF-vdW@BEEF-vdW are shown below. In each calculation, the energy can be obtained as the last column (ENERGY) from the line containing “energy without entropy= NUMBER energy(sigma->0) = ENERGY” — this is the last line indicated by where there is no spacing between the “entropy” and “=” sign:

1. **Initial BEEF-vdW** — Perform a BEEF-vdW calculations (versions prior to 6.4.3 require copying the `vdw_kernel.bindat` file containing the van der Waals kernel) with the following INCAR commands:

```
ENCUT      = 550
LASPH      = .TRUE.
ISMEAR     = -1
SIGMA      = 0.10
GGA        = LIBXC
LIBXC1     = GGA_XC_BEEFVDW
LUSE_VDW   = .TRUE.
ZAB_VDW   = -1.8867
ALGO       = Normal
ISTART     = 0
LWAVE      = .TRUE.
LCHARG    = .FALSE.
```

2. **Non-local van der Waals correlation** — Obtain the correlation arising from the vdW

correlation by performing a BEEF (no vdW) calculation on the BEEF-vdW orbitals (kept in WAVECAR calculated from the previous calculation):

```
ENCUT      = 550
LASPH      = .TRUE.
ISMEAR     = -1
SIGMA      = 0.10
GGA         = LIBXC
LIBXC1     = GGA_XC_BEEFVDW
ALGO        = Eigenval
ISTART     = 1
LWAVE      = .FALSE.
LCHARG     = .FALSE.
```

3. **BEEF exchange and correlation** — Calculate the exchange energy using the BEEF-vdW orbitals.

```
ENCUT      = 550
LASPH      = .TRUE.
ISMEAR     = -1
SIGMA      = 0.10
GGA         = LIBXC
LIBXC1     = GGA_X_BEEFVDW
ALGO        = Eigenval
ISTART     = 1
LWAVE      = .FALSE.
LCHARG     = .FALSE.
```

4. **Exact exchange** — Calculate the exact exchange energy evaluated on the BEEF-vdW orbitals. We note that we use a screened exact exchange energy (due to faster convergence with  $k$ -point mesh) and improved performance (see Section 2):

```
ENCUT      = 550
LASPH      = .TRUE.
ISMEAR     = -1
```

```

SIGMA      = 0.10
GGA        = PE
LHF CALC  = .TRUE.
AEXX       = 1.0
HFSCREEN  = 0.3
ALGO        = Eigenval
ISTART     = 1
LWAVE      = .FALSE.
LCHARG     = .FALSE.

```

An energy is associated with each calculation (where we will call  $E_1$  as the energy obtained from the first calculation) and the final hBEEF-vdW@BEEF-vdW energy is given by the following equation:

$$E_{\text{hBEEF-vdW@BEEF-vdW}} = \underbrace{0.15 E_4}_{\text{HF exchange}} + \underbrace{0.85 E_3}_{\text{BEEF exchange}} + \underbrace{(E_2 - E_3)}_{\text{BEEF correlation}} + \underbrace{(E_1 - E_2)}_{\text{nonlocal vdW}}. \quad (1)$$

We have labeled the contributions each term constitutes in the underbraces. The sum of the first two terms on the right also contain other contributions to the final energy, such as the kinetic and Hartree energy.

Building on top of the first 4 calculations, the RPA energy from PBE orbitals (at smaller energy cutoff) is also required and follows a four-step procedure:

**5. PBE energy and orbitals** — We start a standard PBE calculation using a smaller energy cutoff.

```

ENCUT      = 310
LASPH     = .TRUE.
ISMEAR    = -1
SIGMA     = 0.10
GGA       = PE
LMAXFOCKAE = 4
ALGO      = Normal
ISTART    = 0
LWAVE     = .TRUE.
LCHARG    = .FALSE.

```

6. **Exact exchange from DFT orbitals** — Calculate the (unscreened) exact exchange energy evaluated on the PBE orbitals. This is optional as it is not used in the final calculation, but enables an RPA estimate.

```
ENCUT      = 310
LASPH      = .TRUE.
ISMEAR     = -1
SIGMA      = 0.10
GGA        = PE
LMAXFOCKAE = 4
PRECFOCK  = Normal
LHF CALC  = .TRUE.
AEXX       = 1.0
ALGO        = Eigenval
ISTART     = 0
LWAVE      = .FALSE.
LCHARG     = .FALSE.
```

7. **Obtain full set of unoccupied orbitals** — From the PBE orbitals, perform an exact diagonalization to obtain the full set of unoccupied (and occupied) orbitals needed for the RPA calculation. This requires finding the number of occupied states (numBANDS) by searching within the previous PBE calculation maximum number of plane-waves: numBANDS.

```
ENCUT      = 310
LASPH      = .TRUE.
ISMEAR     = -1
SIGMA      = 0.10
GGA        = PE
LMAXFOCKAE = 4
NBANDS    = numBANDS
ALGO        = Exact
ISTART     = 0
LWAVE      = .TRUE.
```

```
LCHARG = .FALSE.
```

8. **Get RPA correlation energy** — Using the full set of orbitals computed from the preceding calculation, compute the RPA correlation energy. The correlation energy can be obtained from the third column (not the last) of the line containing converged value.

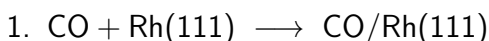
```
ENCUT = 310
LASPH = .TRUE.
ISMEAR = -1
SIGMA = 0.10
LMAXFOCKAE = 4
NBANDS = numBANDS
ALGO = ACFDTR
LOPTICS = .FALSE.
PRECFOCK = Fast
LFINITE_TEMPERATURE = .TRUE.
ISTART = 0
LWAVE = .TRUE.
LCHARG = .FALSE.
```

The final dhBEEF-vdW@BEEF-vdW energy can then be obtained as follows:

$$E_{\text{dhBEEF-vdW@BEEF-vdW}} = \underbrace{0.25 E_4}_{\text{HF exchange}} + \underbrace{0.75 E_3}_{\text{BEEF exchange}} + \underbrace{0.15 E_8}_{\text{RPA correlation}} + \underbrace{0.85 (E_2 - E_3)}_{\text{BEEF correlation}} + \underbrace{(E_1 - E_2)}_{\text{nonlocal vdW}}. \quad (2)$$

## 2. OPTIMIZING THE HBEEF-VDW AND DHBEEF-VDW COEFFICIENTS

As mentioned in the Methods of the main text, there is only one parameter ( $a_h$ ) in hBEEF-vdW and two parameters ( $a_{dh}$  and  $b_{dh}$ ) for dhBEEF-vdW@BEEF-vdW. We used a small set of 7 diverse and representative adsorption systems, dubbed CE7, taken from the CE39 dataset to determine the optimal parameters and ingredients for these NSC-DFAs. These have been selected to represent an assortment of binding mechanisms (including chemisorption and physisorption) on a diverse set of transition metal surfaces. These 7 reactions are as follows:



2.  $\text{NO} + \text{Pd}(111) \longrightarrow \text{NO/Pd}(111)$
3.  $\text{O}_2 + \text{Ni}(100) \longrightarrow 2 \cdot \text{O/Ni}(100)$
4.  $\text{H}_2 + \text{Pt}(111) \longrightarrow 2 \cdot \text{H/Pt}(111)$
5.  $\text{NH}_3 + \text{Cu}(111) \longrightarrow \text{NH}_3/\text{Cu}(111)$
6.  $\text{C}_6\text{H}_6 + \text{Pt}(111) \longrightarrow \text{C}_6\text{H}_6/\text{Pt}(111)$
7.  $\text{H}_2\text{O} + \text{Pt}(111) \longrightarrow \text{H}_2\text{O/Pt}(111)$

### A. Effect of HF screening parameter

In Figures 1 – 4, we highlight the effect of varying the amount of exact exchange (EXX) and RPA correlation on the the mean absolute deviation (weighted per product) on the adsorption energy for the CE7 dataset. We have compared increasing degree of short range-separation ( $\omega$ ) on the EXX for values of 0.0, 0.1, 0.2 and  $0.3 \text{ \AA}^{-1}$ . The amount of EXX controls the  $a$  parameter while the amount of RPA correlation controls the  $b$  parameter.

It can be seen that the overall effect of adding short-range screening does not modify the MAD significantly. When simply varying the % of EXX (with no RPA correlation) in the top panels, increasing the  $\omega$  parameter decreases the overall MAD on CE7, from a MAD of  $25.1 \text{ kJ mol}^{-1}$  to  $22.5 \text{ kJ mol}^{-1}$  for  $\omega = 0.3 \text{ \AA}^{-1}$ . The optimal amount of EXX also increases from 9% to 17%, but remains small and in the values typical of standard hybrid DFAs. Overall, the addition of EXX is beneficial relative to BEEF-vdW, which has an MAD of  $26.9 \text{ kJ mol}^{-1}$  on the CE7 dataset.

When incorporating RPA correlation, we observe significant decreases in the MAD, down to  $\sim 13 \text{ kJ mol}^{-1}$ . There is a smaller dependence on the  $\omega$  parameter, going from an optimal MAD of  $11.5 \text{ kJ mol}^{-1}$  for  $\omega = 0.0 \text{ \AA}^{-1}$  to  $13.4 \text{ kJ mol}^{-1}$  for  $\omega = 0.3 \text{ \AA}^{-1}$ . The optimal EXX also doesn't change, hovering around 24%, while there is some change in the optimal RPA amount, going from 26% for  $\omega = 0.0 \text{ \AA}^{-1}$  to 15% for  $\omega = 0.3 \text{ \AA}^{-1}$ .

With these observations in mind, in our final NSC-DFAs, we used range-separation parameter  $\omega = 0.3 \text{ \AA}^{-1}$  due to its balance at improving the performance of hBEEF-vdW@BEEF-vdW while maintaining a small change on dhBEEF-vdW@BEEF-vdW with respect to full global EXX. As discussed in the main text, there are also several advantages towards incorporating range-separation, namely (1) faster convergence with  $k$ –point mesh and (2) faster convergence with

vacuum amount for the gas-phase molecule. Based on the observations in Figure 4, the optimal value of EXX was chosen to be 17.5% for hBEEF-vdW, while we use a value of 25% for dhBEEF-vdW, together with 15% RPA correlation for dhBEEF-vdW.

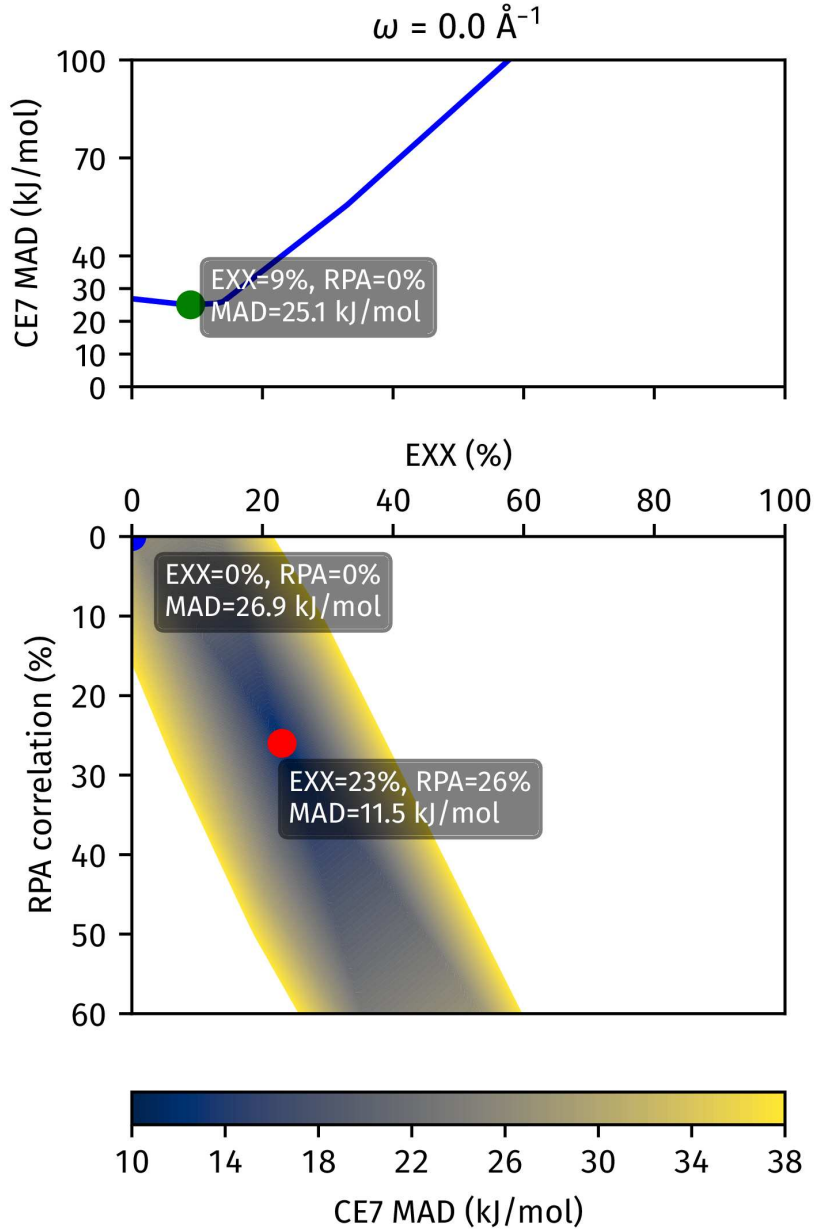


**FIG. 1:** Change in mean absolute deviation (MAD) on the CE7 dataset as a function of global exact exchange and RPA correlation using PBE orbitals for dhBEEF-vdW@BEEF-vdW. The absolute differences computed in the MAD is weighted per product.

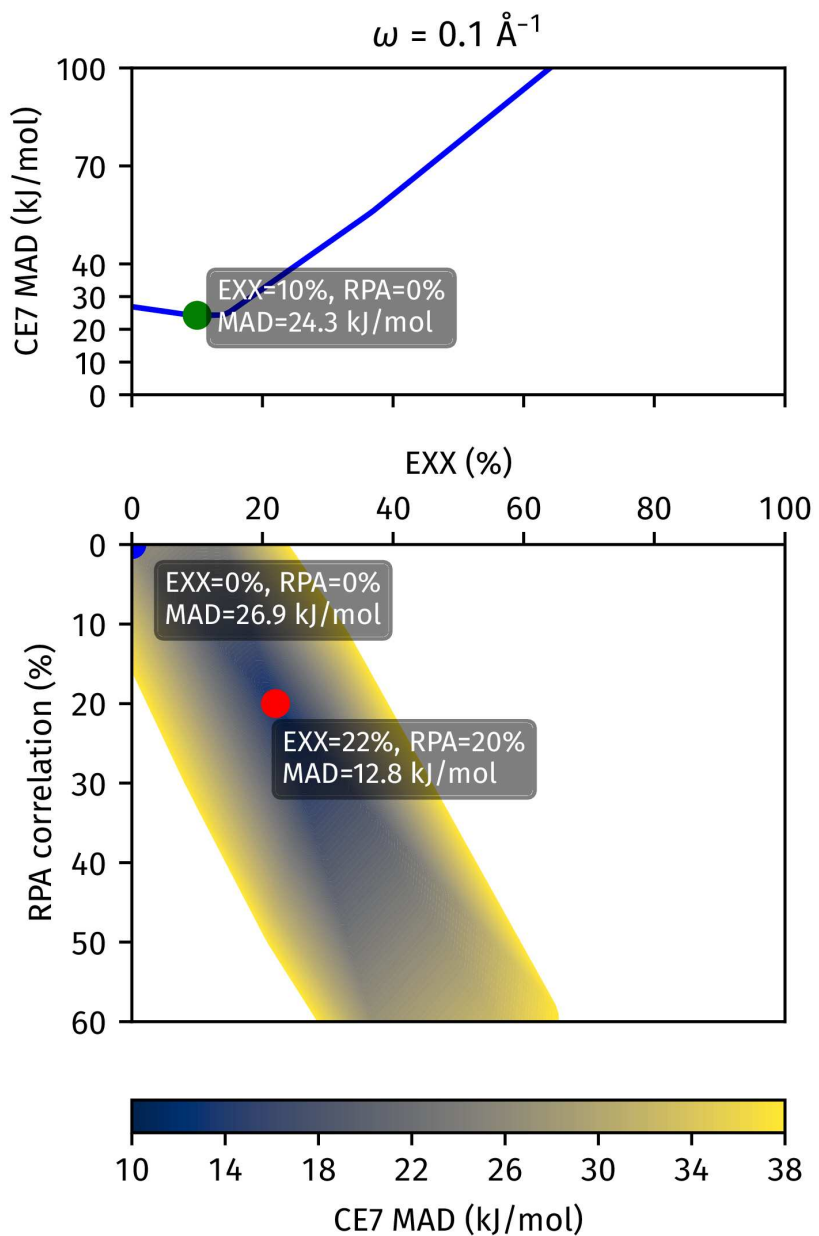


**FIG. 2:** Change in mean absolute deviation (MAD) on the CE7 dataset as a function of screened exact exchange with  $\omega = 0.1 \text{ \AA}^{-1}$  and RPA correlation using PBE orbitals for dhBEEF-vdW@BEEF-vdW. The absolute differences computed in the MAD is weighted per product.

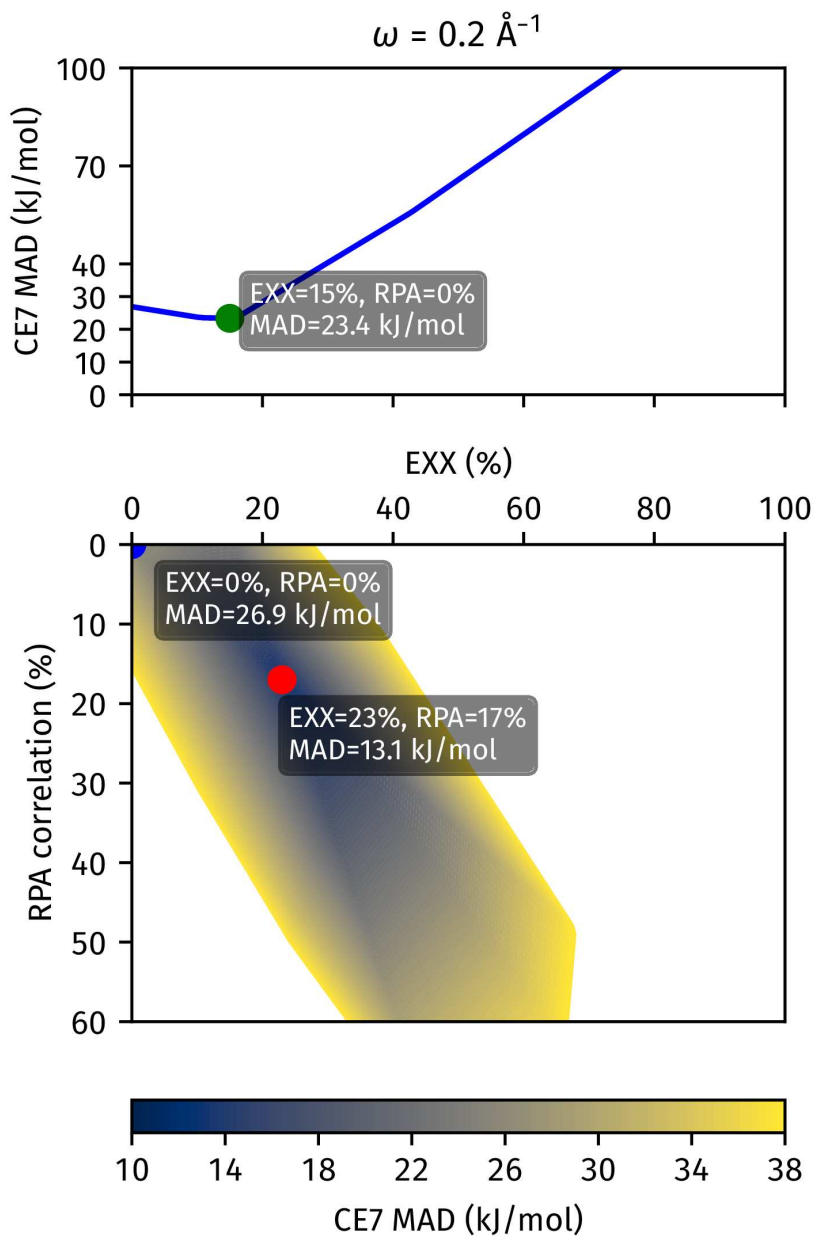


**FIG. 3:** Change in mean absolute deviation (MAD) on the CE7 dataset as a function of screened exact exchange with  $\omega = 0.2 \text{ \AA}^{-1}$  and RPA correlation using PBE orbitals for dhBEEF-vdW@BEEF-vdW. The absolute differences computed in the MAD is weighted per product.

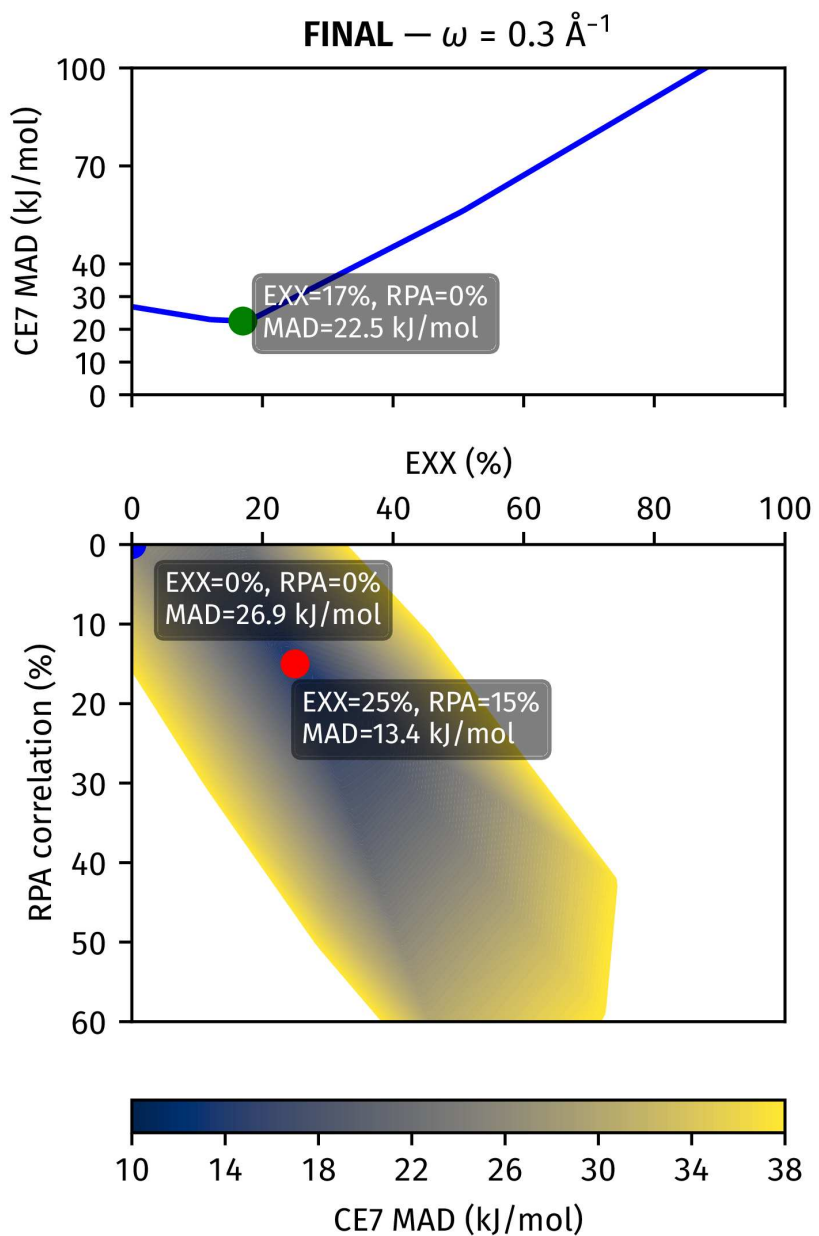


**FIG. 4:** Change in mean absolute deviation (MAD) on the CE7 dataset as a function of screened exact exchange with  $\omega = 0.3 \text{ \AA}^{-1}$  and RPA correlation using PBE orbitals for dhBEEF-vdW@BEEF-vdW. The absolute differences computed in the MAD is weighted per product.

## B. PBE vs. BEEF-vdW orbitals for RPA correlation

We also originally considered utilizing RPA on BEEF-vdW orbitals, as opposed to PBE orbitals for the RPA correlation component. As shown in Figure 5, this leads to overall higher MAD of  $16.4 \text{ kJ mol}^{-1}$  with RPA@BEEF-vdW correlation compared to  $13.4 \text{ kJ mol}^{-1}$  for RPA@PBE correlation. Thus, we opted to stick to RPA@PBE correlation. Practically, this does not add additional costs or steps in dhBEEF-vdW@BEEF-vdW in Section 1 because the initial DFT calculation (whether PBE or BEEF-vdW) had to be re-performed at a smaller energy cutoff and cannot be inherited from the original BEEF-vdW calculations in Step 1.

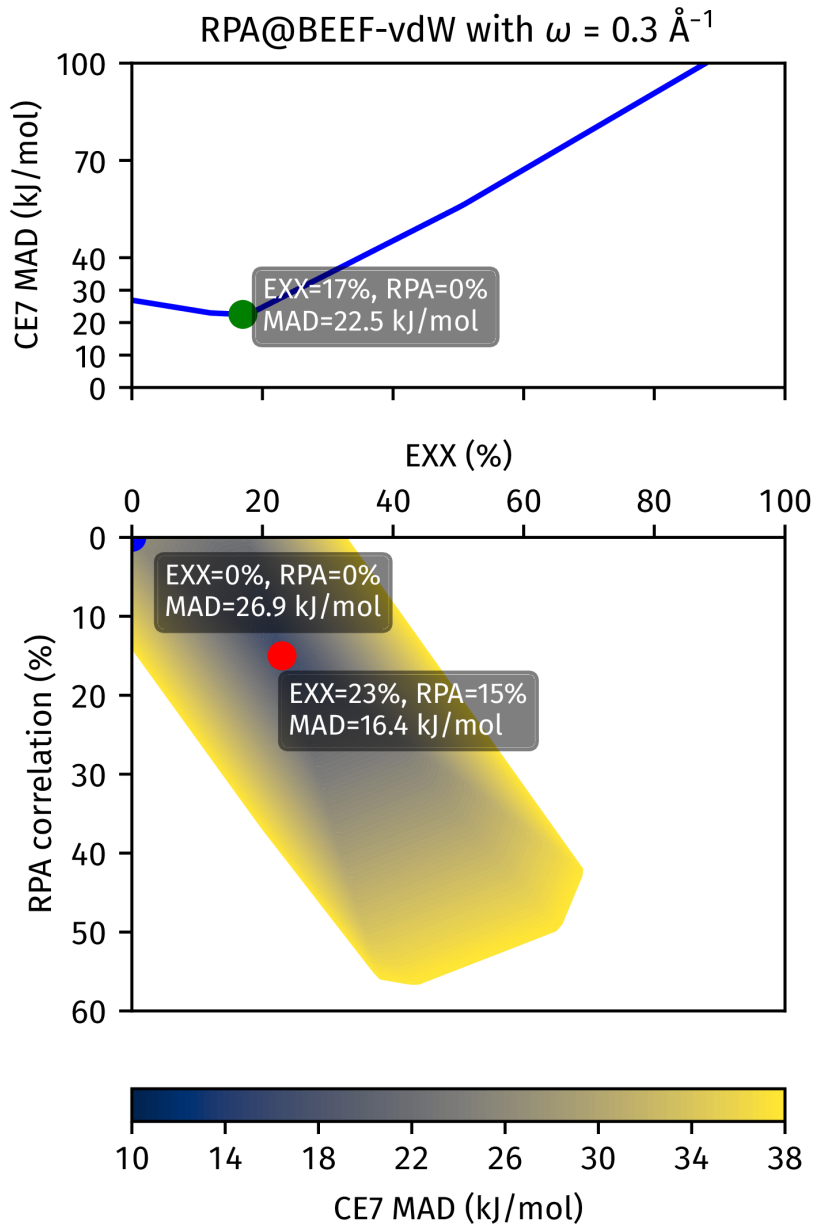


**FIG. 5:** Change in mean absolute deviation (MAD) on the CE7 dataset as a function of screened exact exchange with  $\omega = 0.3 \text{ \AA}^{-1}$  and RPA correlation using the BEEF-vdW orbitals for dhBEEF-vdW@BEEF-vdW. The absolute differences computed in the MAD is weighted per product.

### 3. QUALITATIVE IMPROVEMENTS ON CO ADSORPTION PUZZLE

In this section, we discuss briefly the positive impact both exact exchange and RPA correlation have on the the CO adsorption puzzle for Pt(111). We will aim to highlight why there is the expected improvements for CO on Pt(111) when using hBEEF-vdW@BEEF-vdW by comparing its density of states to BEEF-vdW and RPA(GW).

#### A. Effect of exact exchange

In Figure 6, we show the effect of exact exchange (screened with  $\omega = 0.3 \text{ \AA}^{-1}$ ) and RPA correlation energy on the relative energy between the top and hollow sites for CO on Pt(111). Here, the effect of both EXX and RPA correlation is to increase the stability of the top site. This is not unexpected given the preference of RPA@PBE for the top site.

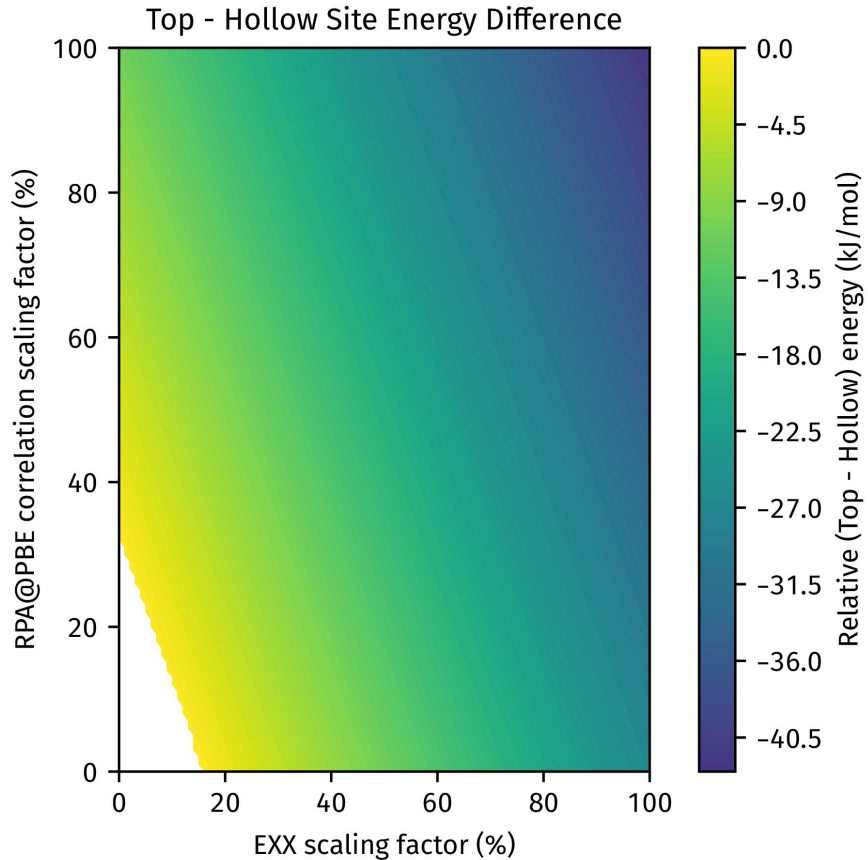


**FIG. 6:** Change in relative energy between the top and hollow site for CO adsorbed on Pt(111) as a function of screened exact exchange with  $\omega = 0.3 \text{ \AA}^{-1}$  and RPA correlation using PBE orbitals. Positive values (i.e., where the hollow site is more stable) are given as white.

The most interesting result is that without RPA@PBE correlation, we can stabilize the top site in hBEEF-vdW@BEEF-vdW (corresponding to the x-axis of Figure 6). There is a strong dependence on the amount of EXX, which pushes the stability to the top site at  $\sim 15\%$  or beyond. As discussed in the main text, standard self-consistent hybrid DFAs do not stabilize the top site as the de-stabilization of the hollow-site from decreased electron back-donation is counteracted by stabilization from decreased steric repulsion. It arises because self-consistent hybrids localize electrons on the metal atoms much more compared to semilocal DFAs. We do not have this competing effect within this work as the electron density is kept at the level of the GGA BEEF-vdW. In addition, as discussed in the next section, the stabilizing effect from decreased back-donation is maintained with hBEEF-vdW@BEEF-vdW.

## B. Changes in the density of states for CO on Pt(111)

The relative stability of the top and hollow CO adsorption sites is often attributed to a competition between several effects [2]. The top site is stabilized by  $\sigma$  bonds that form between the CO molecule and metal surface due to donation of electrons from the  $5\sigma$  orbital to the empty metal states (predominantly  $dz^2$ ). The hollow-site is stabilized by back-donation from the metal  $d$  orbitals into the anti-bonding  $2\pi^*$  orbitals of the CO molecule, weakening the C–O bond while strengthening the bond between the CO molecule and surrounding three metal atoms. For this site, due to the close proximity of the CO molecule to several metal elements, the effect of steric repulsion is also important.

Semilocal DFAs (such as LDA, GGAs and metaGGAs) have a tendency to underestimate the HOMO-LUMO gaps of bandgaps of molecules and materials, respectively. This tends to place the  $2\pi^*$  orbitals of the CO molecule closer to the Fermi level, thus strengthening the bonding of the hollow-site, hence unphysically favoring the hybrid sites.

The effect of hybrid functionals is to shift the  $2\pi^*$  orbitals further above the Fermi level. This decreases the amount of back-donation, hence weakening the bond to the hollow site and disfavoring the hollow site. However, it also localizes the electron density on the metal atoms, and this in turn decreases the amount of steric repulsion they give, favoring the hollow site. Stroppa and Kresse [2] showed that while this favors the top site for Cu(111) and Rh(111), it remains unable to resolve this for Pt(111). They concluded that the “inclusion of 25% non-local exchange, bare or long-range screened, hardly improves the description of CO adsorption on metal surfaces.”

The use of our hybrid NSC-DFAs resolves this issue because it uses an electron density coming from a semilocal DFA, hence preventing the localization of electron density on metal atoms. This means that the main effect is to weaken the bond between the CO molecule and metal surface for the hollow site. In Figure 7, we show that the position of the  $2\pi^*$  orbital moves upwards as a function of non-local exchange in the system, explaining the steady stabilization of the top site as a function % of EXX. While BEEF-vdW by itself predicts the  $2\pi^*$  position to be below that from GW(RPA), the inclusion of screened exact exchange in hBEEF-vdW@BEEF-vdW brings its position closer to that of the  $2\pi^*$  position. We note that there remain some qualitative differences in the features of DOS, such as broadening of the  $d$ -band and also  $2\pi^*$  orbitals.

#### 4. TIMING RATIOS BETWEEN RPA, EXX AND DFT

In Table 1, we highlight the relative costs to perform the BEEF-vdW calculation (Step 1 in Section 1), EXX calculation (Step 4) and RPA correlation calculation (Step 8), representing the most costly steps in the hBEEF-vdW@BEEF-vdW and dhBEEF-vdW@BEEF-vdW calculations. It can be seen that the EXX calculation is on average  $20 \times$  more expensive than the BEEF-vdW calculation, while the RPA correlation calculation is around  $2 \times$  the cost of the EXX calculation. Both are cost efficient, especially given the fact that a normal self-consistent hybrid DFA would cost  $\sim 50 \times$  the cost of the hBEEF-vdW@BEEF-vdW since they may require that number of self-consistent field cycles to reach convergence.

---

[1] S. Lehtola, C. Steigemann, M. J. T. Oliveira, and M. A. L. Marques, Recent developments in libxc — A comprehensive library of functionals for density functional theory, [SoftwareX 7, 1 \(2018\)](#).

[2] A. Stroppa and G. Kresse, The shortcomings of semi-local and hybrid functionals: What we can learn from surface science studies, [New J. Phys. 10, 063020 \(2008\)](#).

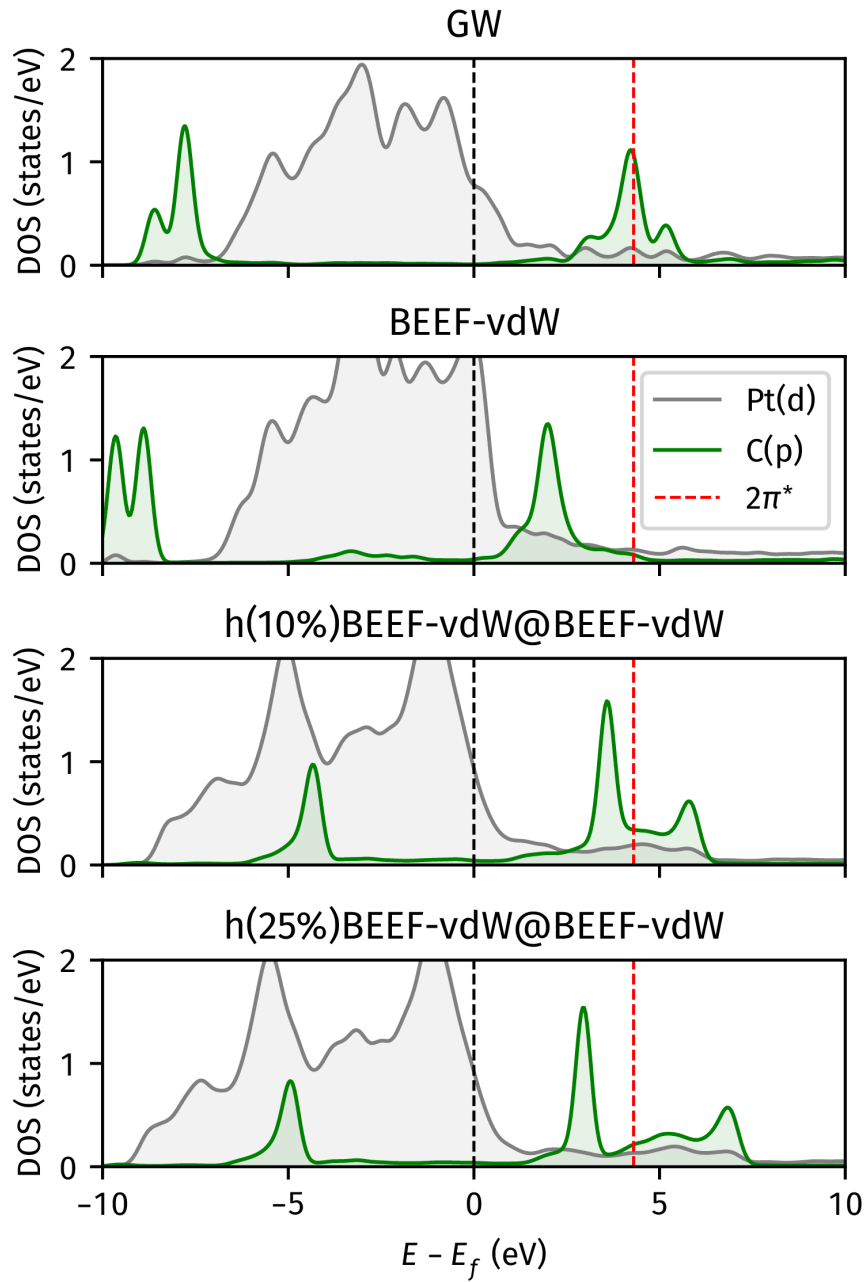


**FIG. 7:** Comparison of the electronic density-of-states (DOS) predicted by GW(RPA), BEEF-vdW and hBEEF-vdW@BEEF-vdW. For hBEEF-vdW@BEEF-vdW, the amount of exact-exchange has been varied from 10% to 25%. Here, global exact exchange is used in hBEEF-vdW@BEEF-vdW as it was not possible to obtain the DOS when using screened exact exchange. The DOS has been projected on the Pt *d* orbitals (subsequently normalized by the number of Pt atoms) and on the C *p* orbitals. The Fermi level is highlighted with a dotted black line while the position of the  $2\pi^*$  orbital from GW(RPA) on the CO atom is indicated with the red line.

**TABLE 1:** Ratio between the computational cost of EXX and RPA calculations compared to BEEF-vdW for the CE39 dataset.

	BEEF-vdW	EXX	RPA
CO + Ni(111) → CO/Ni(111)	1	18	24
CO + Pt(111) → CO/Pt(111)	1	23	36
CO + Pd(111) → CO/Pd(111)	1	25	45
CO + Pd(100) → CO/Pd(100)	1	27	56
CO + Rh(111) → CO/Rh(111)	1	18	52
CO + Ir(111) → CO/Ir(111)	1	15	29
CO + Cu(111) → CO/Cu(111)	1	22	35
CO + Ru(001) → CO/Ru(001)	1	14	73
CO + Co(001) → CO/Co(001)	1	18	24
NO + Ni(100) → N/Ni(100) + O/Ni(100)	1	16	28
NO + Pt(111) → NO/Pt(111)	1	18	33
NO + Pd(111) → NO/Pd(111)	1	22	43
NO + Pd(100) → NO/Pd(100)	1	25	58
O <sub>2</sub> + Ni(111) → 2O/Ni(111)	1	17	26
O <sub>2</sub> + Ni(100) → 2O/Ni(100)	1	16	28
O <sub>2</sub> + Pt(111) → 2O/Pt(111)	1	16	30
O <sub>2</sub> + Rh(100) → 2O/Rh(100)	1	16	66
H <sub>2</sub> + Pt(111) → 2H/Pt(111)	1	24	45
H <sub>2</sub> + Ni(111) → 2H/Ni(111)	1	17	27
H <sub>2</sub> + Ni(100) → 2H/Ni(100)	1	16	29
H <sub>2</sub> + Rh(111) → 2H/Rh(111)	1	18	63
H <sub>2</sub> + Pd(111) → 2H/Pd(111)	1	23	50
I <sub>2</sub> + Pt(111) → 2I/Pt(111)	1	24	38
CH <sub>2</sub> I <sub>2</sub> + Pt(111) → CH/Pt(111) + H/Pt(111) + 2I/Pt(111)	1	24	44
CH <sub>3</sub> I + Pt(111) → CH <sub>3</sub> /Pt(111) + I/Pt(111)	1	24	44
NH <sub>3</sub> + Cu(100) → NH <sub>3</sub> /Cu(100)	1	20	33
CH <sub>3</sub> I + Pt(111) → CH <sub>3</sub> I/Pt(111)	1	23	36
CH <sub>3</sub> OH + Pt(111) → CH <sub>3</sub> OH/Pt(111)	1	23	42
CH <sub>4</sub> + Pt(111) → CH <sub>4</sub> /Pt(111)	1	23	43
C <sub>2</sub> H <sub>6</sub> + Pt(111) → C <sub>2</sub> H <sub>6</sub> /Pt(111)	1	17	31
C <sub>3</sub> H <sub>8</sub> + Pt(111) → C <sub>3</sub> H <sub>8</sub> /Pt(111)	1	18	32
C <sub>4</sub> H <sub>10</sub> + Pt(111) → C <sub>4</sub> H <sub>10</sub> /Pt(111)	1	18	33
C <sub>6</sub> H <sub>6</sub> + Pt(111) → C <sub>6</sub> H <sub>6</sub> /Pt(111)	1	16	28
C <sub>6</sub> H <sub>6</sub> + Cu(111) → C <sub>6</sub> H <sub>6</sub> /Cu(111)	1	25	29
C <sub>6</sub> H <sub>6</sub> + Ag(111) → C <sub>6</sub> H <sub>6</sub> /Ag(111)	1	34	53
C <sub>6</sub> H <sub>6</sub> + Au(111) → C <sub>6</sub> H <sub>6</sub> /Au(111)	1	31	44
C <sub>6</sub> H <sub>10</sub> + Pt(111) → C <sub>6</sub> H <sub>10</sub> /Pt(111)	1	17	31
H <sub>2</sub> O + Pt(111) → H <sub>2</sub> O/Pt(111)	1	23	38
H <sub>2</sub> O + OPt(111) → H <sub>2</sub> OOH/Pt(111)	1	18	28